

# Department of Precision and Microsystems Engineering

## Photonic Crystal Nanobeam Cavities as Hydrogen Sensors

L.J.F. Leermakers

Report no : 2022.012  
Coach : Dr. Ir. R.A. Norte and Ir. M.H.J. de Jong  
Professor : Prof. Dr. Ir. P.G. Steeneken  
Specialisation : Engineering Dynamics  
Type of report : Master Thesis  
Date : May 12<sup>th</sup>, 2022



# Photonic Crystal Nanobeam Cavities as Hydrogen Sensors

## Master's Thesis

by

**L.J.F. Leermakers**

A thesis submitted in fulfillment of the requirements  
for the degree of Master of Science in Mechanical Engineering in the  
Dynamics of Micro and Nanosystems Group  
Department of Precision and Microsystems Engineering

Student number: 4967933

Project duration: March 1<sup>st</sup>, 2021 – May 12<sup>th</sup>, 2022

Thesis committee: Dr. Ir. R. A. Norte TU Delft, supervisor  
Prof. Dr. Ir. P. G. Steeneken TU Delft, supervisor  
Ir. M. H. J. De Jong TU Delft, daily supervisor



# *Abstract*

Due to the demand for renewable energies, gasses like H<sub>2</sub> need to be detected with sensitive, accurate and fast detectors. The US Department of Energy has made a list of requirements that H<sub>2</sub> sensors need to fulfill of which the minimum detectable concentration (0.1%) and the reaction time (one second) are challenging for current hydrogen sensors, particularly for low-power and low-cost mass-produced sensors. This thesis covers the design and simulation of a photonic crystal nanobeam cavity sensor, using the Pt-catalyzed WO<sub>3</sub> as a H<sub>2</sub> sensitive material. The thicknesses of both layers show a trade-off between the minimally detectable concentration and the reaction times, resulting in a cavity with sensitivity of almost  $40 \frac{nm}{RTU}$  and a Q factor varying between  $5 \cdot 10^5$  and  $5 \cdot 10^4$  depending on how much catalyst is required to meet the one second reaction time performance target. Based on the conservative assumptions regarding the reaction times of the sensor, the 0.1% performance target is almost achieved. This means that if in practice, any of the layer thicknesses show to be more favourable than assumed in this thesis, together with the fact that for optical sensors there is no risk of sparks, the photonic crystal nanobeam cavity as a H<sub>2</sub> sensor shows to be a good fit for a high performance, low-cost, mass-produced H<sub>2</sub> sensor that meets the DoE performance targets.



# *Acknowledgements*

During this thesis I have learned many things about myself and what its like to do research. I could not have done this alone which is why I would like to thank some people. First of all, I want to thank Matthijs as my daily supervisor. Being my first point of contact, Matthijs was always there to answer my questions, discuss and give me feedback on my progress. Before each meeting I felt stuck with many questions which where all answered during the meeting, keeping me motivated to continue. I want to thank Peter and Richard for giving my an opportunity to do this project and introducing me to the world of optics. The weekly meetings with the DMN group governed by Peter, have been inspirational and educational as it has given me a better insight in how to do research. The weekly meetings with the Norte Lab governed by Richard, have been just as helpfull. Being able to share my progress and have small-group discussions with fellow students and PhD'ers has helped me to be more critical about my work. Next to that, I would like to thank Richard for our discussions. Richard's creative mind and eagerness for knowledge has been inspiring and motivational. Furthermore, I want to thank my good friend Ids for studying my work and being a discussion partner. Ids has helped me with showing me how my work is perceived by another mechanical engineer who is not familiar with this field. Last but not least, I want to thank Teuntje for her mental support during the whole process, as she has always been there for me for as long as I can remember.

*L.J.F Leermakers  
Delft, May 2022*



# Contents

1	Introduction	1
2	Background	5
2.1	WO <sub>3</sub> H <sub>2</sub> reaction	5
2.2	Refractive index	6
2.2.1	H <sub>x</sub> WO <sub>3</sub>	6
2.2.2	Pt	7
2.3	Optical Cavity Sensors	7
2.3.1	Photonic Crystal Nanobeams	9
2.3.2	Sensor Performance	11
2.4	Reaction Times	12
3	Methods	17
3.1	Simulation	17
3.1.1	Optimization	17
3.2	Initial H <sub>2</sub> Sensor Design	19
3.3	The Flow of the Results Section	23
4	Results	25
4.1	Optimization	25
4.2	The Platinum Layer	27
4.3	Nanobeam with Limited Number of Nanoparticles	29
4.4	Simplified Nanobeam	31
4.4.1	$\kappa$ comparisons	31
4.4.2	The WO <sub>3int</sub> Layer Simulations	33
4.5	Performance Comparison	35
5	Conclusion	37
A	Appendix	39
A.1	Absorption versus Rayleigh Scattering	39
	Bibliography	41



# 1

## Introduction

For the last decades, the demand for renewable energies like hydrogen ( $H_2$ ) has been increasing due to global warming. A report made by the International Energy Agency for the G20 in 2019, states that the demand for  $H_2$  has grown more than threefold since 1975 and explains about the usages of  $H_2$  [1]. One of the many challenges to be tackled in order to make the use of  $H_2$  safe, is the ability to detect  $H_2$  with great precision and speed [2, 3]. To get a good understanding of what specifications a  $H_2$  sensor should comply with, the US Department of Energy (DoE) has set performance targets for  $H_2$  gas sensors, to quantify whether a sensor meets all the codes and standards for safe and compatible use in a commercial and/or infrastructure setting, table 1.1 [4].

Table 1.1: DoE performance targets for  $H_2$  sensors [4].

Performance target	Quantity
Measurement Range	0.1% - 10%
Operating Temperature	-30° - 80°
Reaction Time	<1 s
Accuracy	5% of full scale
Gas Environment	Ambient Air, 10% - 98% relative humidity range
Lifetime	10 years

Commercially available  $H_2$  sensors report about reaction times close to 1 second and  $H_2$  concentrations down to 1% [5]. Because these sensors do not meet all the DoE targets, research is done so that new sensors can be made which are more sensitive and have a faster reaction time. In 2020, Darmadi et al. [3] have summarized a large amount of literature with respect to these targets to obtain a list of the most promising high performance sensor designs. The paper shows that there are many sensors able to detect low concentrations of  $H_2$  but that the speed in which the sensors operates is the bottleneck of  $H_2$  sensing. Many of these sensors use metals like palladium (Pd), platinum (Pt), gold (Au) and oxides like tungsten trioxide ( $WO_3$ ), tin oxide ( $SnO_2$ ) and molybdenum oxide ( $MoO_3$ ) to measure  $H_2$ . These materials are well-suited as their material properties like resistance [6, 7], colour [7, 8], size [9], transmission [8] and refractive index [10, 11] change significantly when in contact with  $H_2$ . Amongst the best performing sensors from literature, Chen et al. [12] detect  $H_2$  concentrations down to 0.1% in 0.3 seconds by measuring the electrical resistance of Pt coated  $SnO_2$  nanorods. Mattoni et al. [7] have made a high performance sensor from  $WO_3$  coated with Pt nanoparticles that measures 100 ppm  $H_2$  within one second at 65°C by measuring the change of electrical resistivity in the  $WO_3$ . However, like Chen et al., Mattoni et al. and many other high sensitivity papers listed in the literature summary from Darmadi et al., the sensing principle that is used is based on measuring resistance or any other form of electricity which introduces the risk of sparks that can ignite  $H_2$  when its volumetric concentration

in air is 4% or higher [13, 14] and the energy from the spark is more than 0.01 mJ [1, 15]. Comparing H<sub>2</sub> with gasoline, H<sub>2</sub> requires 80 times less energy to ignite [16].

Optical sensors do not use electricity at the measuring location, eliminating the risk of sparks. Optical sensors work by shining light onto a surface or substance that changes colour, reflectivity or other properties when it interacts with something that we want to detect and can be distinguished into three categories: reflective, transmissive and cavity sensors. Xie et al. [17] and Nau et al. [18] have designed a sensor where the reflected light from a surface covered with WO<sub>3</sub> and Pt is measured as it is a function of the H<sub>2</sub> concentration. The Pt is a catalyst for the reaction between the WO<sub>3</sub> and H<sub>2</sub>,



The exact functioning of this chemical reaction is given in section 2.1. Zhao et al. [19] and Wang et al. [20] use a similar principle where an optical fiber is coated with WO<sub>3</sub> and Pd or Pt. A change in the refractive index of the WO<sub>3</sub> changes the sensor output which can be related to a certain H<sub>2</sub> concentration. Hsu et al. [21] have designed an optical H<sub>2</sub> sensor with WO<sub>3</sub> and Pt that uses the change in transmittance to measure H<sub>2</sub>. Just as the Pt, Pd is a catalyst for the reaction as well. Next to that, Pd on its own is also used to make H<sub>2</sub> sensors with [22]. When exposed to H<sub>2</sub>, its permittivity changes which has an effect on for example the transmittance and reflectance of the material [23, 24].

What almost all of these papers have in common, is the use of WO<sub>3</sub> together with a catalyst like Pt or Pd. WO<sub>3</sub> is a H<sub>2</sub> sensitive material since its refractive index goes from 2.0 [10, 11] to 2.4 [25, 26], its colour goes from white to blue [8] when exposed to H<sub>2</sub> and the optical absorption is practically zero for low concentrations of H<sub>2</sub> at telecom wavelengths (1500 nm). Another material very similar to WO<sub>3</sub> is MoO<sub>3</sub> as both its refractive index and colour change as well when in contact with H<sub>2</sub> [27]. MoO<sub>3</sub> is less favourable to use though, as its refractive index only goes from 1.9 to 2.0 instead of 2.0 to 2.4 [28].

The sensing principles in the papers named above, have limited light-matter interaction. This is because light interacts just once with the material when it is reflected or transmitted. This leads to the third type of optical sensor, an optical cavity sensor. An optical cavity sensor is where two opposed highly reflecting mirrors are placed such that light can resonate inbetween. As the light resonates back and forth in the cavity, the light-matter interaction is enhanced because the light travels through the material multiple times. Next to that, the concept of an optical cavity allows to concentrate light in a small area. This allows for only having to place the H<sub>2</sub> sensitive material at that location. Albeit not a H<sub>2</sub> but a H<sub>2</sub>S sensor, Afsari et al. [29] have designed such an optical cavity sensor by adding a thin layer of WO<sub>3</sub> on top of a Silicon (Si) two-dimensional photonic crystal (PhC) slot-cavity, figure 1.1. A PhC is a subwavelength scale periodic arrangement of different RI materials [30] which in an application like in figure 1.1 can be used as a mirror and is explained more about in section 2.3.1. The PhC in figure 1.1 makes that light resonates back and forth in what is called the slot cavity, the green region in the figure.

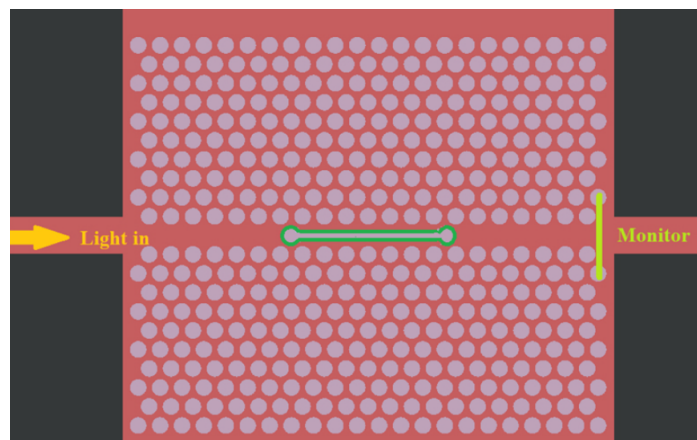


Figure 1.1: The PhC of Afsari et al. [29] where the red material is the WO<sub>3</sub> coated Si and the light grey is air.

Another PhC cavity design is a nanobeam which has more of a one-dimensional structure and is known to achieve resonances with low optical loss such that the light-matter interaction is high. Figure 1.2 shows how such a geometry looks like and in section 2.3.1, a more in-depth understanding of a nanobeam is given. One of the big advantages of sensors like in figure 1.1 and 1.2 is that these are low-power, low-cost and easy to mass-produce with the use of etching as they are two-dimensional structures. In this thesis, the PhC nanobeam cavity will be used to research its performance as a  $H_2$  sensor. This performance is measured based on the performance measures created by the DoE, table 1.1 and will determine how low concentrations the sensor can measure and what the response time of the sensor becomes.



Figure 1.2: Improved PhC nanobeam design where tapered holes are added in the defect region to reduce the scattering losses and confine the light.

Apart from the conclusion and this introduction, this thesis consists of three chapters: the background, methods and results, sections 2, 3 and 4 respectively. In the background, several concepts are explained like the chemical reaction of  $WO_3$  and  $H_2$ , the refractive index, what optical cavity sensors are (specifically PhC nanobeam cavities), how to quantify their performances and finally a small literature research on the reaction times of  $WO_3$ . In the methods is explained what techniques are used to obtain the performance of the sensor like simulations, optimizations, what nanobeam design is used and a flowchart of how the result section is build up is given. Finally, in the results, simulations are given and discussed. There are some limitations regarding the simulations because of computational limits which are resolved via workarounds and shown in the results as well. The final performance of the most optimal design is also given, discussed and compared.



# 2

## Background

In the following sections, first the  $\text{WO}_3$   $\text{H}_2$  reaction is further explained, then a more in-depth overview of the refractive index is given. The sections following after that explain what optical cavity sensors are with a focus on PhC nanobeam cavities and how the performance can be quantified. Finally, a literature research on the reaction times of  $\text{H}_2$  with  $\text{WO}_3$  is given.

### 2.1. $\text{WO}_3$ $\text{H}_2$ reaction

$\text{WO}_3$  is a transition metal oxide which has a gasochromic reaction with  $\text{H}_2$  [22] forming hydrogen tungsten bronze ( $\text{H}_2\text{WO}_3$ ) with Platinum (Pt) or Palladium (Pd) as a catalyst [7, 31, 32],



The value of  $x$  varies depending on the amount of  $\text{H}_2$  present. When the  $\text{H}_2$  comes into contact with the  $\text{WO}_3$  and the catalyst, the catalyst helps split the  $\text{H}_2$  molecules into dissociated H atoms which then react with the  $\text{WO}_3$  changing the oxidation state (charge) of some W ions from +6 to +5 [20, 22, 31, 33]. Comparing catalysts Pd and Pt, they both dissociate  $\text{H}_2$  with equal performance. However,  $\text{H}_2$  is much less soluble in Pt than it is in Pd meaning that H atoms are more likely to stick to the Pd than to the Pt. This is not desired as the H atoms should penetrate into the  $\text{WO}_3$  and not stick to the catalyst. Next to that, Pd increases in size as it absorbs H atoms. If the Pd layer is for example attached to a Si layer, when the Pd layer grows it can crack because the Si layer doesn't grow as well. These two main aspects make that Pt is favourable over Pd [34, 35]. Important to note is that the reaction can also occur without the catalyst, however this reaction will then be extremely slow compared to the reaction with the catalyst. Without the catalyst the  $\text{H}_2$  molecules need to dissociate themselves which only happens when significant energy is added to the reaction which is something that almost not happens at room temperature [36].

There are two ways of combining Pt with the  $\text{WO}_3$  which is either by mixing them together to form one homogenous mixture or by placing the Pt on top of the  $\text{WO}_3$ , figures 2.1a and 2.1b respectively [7, 17, 37]. Note that in figure 2.1b the Pt is not a uniform layer but a collection of nanometre-sized particles which is expected when depositing such small amounts of material [7]. Because the  $\text{H}_2$  molecules need to dissociate into H atoms before they can interact with the  $\text{WO}_3$  lattice, having the nanoparticles on top is favourable over having the Pt mixed in the  $\text{WO}_3$  as the  $\text{H}_2$  molecules in the outside environment can reach each Pt nanoparticle with ease in figure 2.1b and not in figure 2.1a [7, 25]. Next to that, the fact that the Pt in figure 2.1b is a collection of nanoparticles instead of a single uniform layer is favourable as well as the nanoparticles have a larger surface to volume ratio compared to a single layer which results in more surface where the  $\text{H}_2$  can react with. Why the amount of Pt is so little that it isn't a uniform layer and how different setups of  $\text{WO}_3$  plus a catalyst (Pd or Pt) perform, is researched in section 2.4 where a literature research is done on the reaction times of  $\text{H}_2$  with  $\text{WO}_3$  to find a setup which meets the one second reaction time performance target.



Figure 2.1: Two different ways to combine the catalyst Pt with the  $\text{WO}_3$ ; (a) Pt inside the  $\text{WO}_3$  and (b) Pt on top of the  $\text{WO}_3$ .

## 2.2. Refractive index

The refractive index is what defines the physics of a PhC and is the sensing mechanism of the  $\text{WO}_3$  in the sensor which is why in this section is explained what the refractive index exactly is. The refractive index is a complex number ( $n \pm i\kappa$ ) and used to describe how light travels through a medium. The real part ( $n$ ) is defined as the speed of light in vacuum ( $c$ ) over the phase velocity in a medium ( $v$ ) and describes how fast light travels through this medium,

$$n = \frac{c}{v}. \quad (2.2)$$

If for example  $n$  is equal to 2, light travels twice as slow through that medium as it would in vacuum.  $n$  describes the refraction of light and is what defines the working of a PhC and is used as the sensing principle for resonant refractive index sensors which is explained more about in section 2.3.

The imaginary part  $\kappa$  is often called the extinction or attenuation coefficient and describes how much optical energy is absorbed in the material. Using the Beer-Lambert law [38], the light intensity ( $I$ ) in a material can be given as following,

$$I = I_0 e^{-4\pi\kappa x_w / \lambda_0} \quad (2.3)$$

where  $x_w$  describes the depth at which  $I$  needs to be determined and  $\lambda_0$  is the wavelength in vacuum. The equation shows that the light intensity decreases exponentially as  $x_w$  increases which can be expected of absorption in a material.

### 2.2.1. $\text{H}_x\text{WO}_3$

The refractive index of  $\text{WO}_3$  goes from 2.0 to 2.4 as  $\text{WO}_3$  turns into  $\text{H}_x\text{WO}_3$  when  $\text{H}_2$  is added and the absorption is practically zero. Both Green et al. [25] and Hussain et al. [26] have done experiments on this refractive index as a function of  $x$ , figure 2.2 showing very similar results. The change in refractive index is linear, except around  $x = 0.1$ . This means that when the refractive index is equal to any value between 2.2 and 2.4,  $x$  can be either between 0.08 and 0.1 or 0.1 and 0.13. Because  $x$  is a function of the  $\text{H}_2$  concentration, it means that for certain concentrations of  $\text{H}_2$  there is no difference in cavity mode as they both occur at the same refractive index.

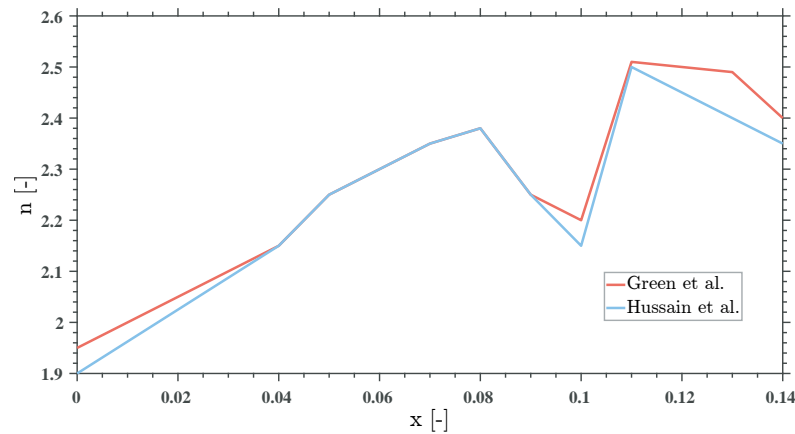


Figure 2.2: The refractive index ( $n$ ) of  $\text{H}_x\text{WO}_3$  measured as a function of  $x$  according to two different papers by Green et al. [25] and Hussain et al. [26].

Another important finding from figure 2.2 is that the maximal refractive index is almost already reached before the dip at  $x = 0.08$ . This is favourable for using the change of refractive index as a sensing mechanism as more change in refractive index in the material means more effect on sensor readout. However, to say anything about how the refractive index of  $H_xWO_3$  changes as a function of the  $H_2$  concentration, a relation for  $x$  and the  $H_2$  concentration has to be determined. Both measurements from figure 2.2 measure at a maximum value of  $x = 0.14$  and report that the H atoms are placed in the  $H_xWO_3$  actively by adding energy to the chemical reaction. For sensors, the H atoms diffuse into the lattice passively. Jung et al. [39] have done experiments on  $H_xWO_3$  where the material is exposed to 100%  $H_2$  at atmospheric pressure resulting in  $x = 0.1$  as where the  $WO_3$  lattice is saturated with H atoms. It is not mentioned for what period of time the  $H_xWO_3$  is exposed to the  $H_2$  but the assumption is made that it was long enough for the reaction to fully occur. This means that looking at figure 2.2, when  $x$  goes from 0 to 0.1, the  $H_2$  concentration goes from 0 to 100% while the maximum refractive index of 2.4 is already reached at  $x = 0.08$ . However, to make a conservative assumption, the relation between the  $H_2$  concentration and refractive index is assumed to be linearly going from 2.0 to 2.4 for a concentration going from 0 to 100%.

### 2.2.2. Pt

Pt is a metal with high absorption which has a large impact on the optical losses in the sensor, table 2.1 where different findings for the refractive index at 1500 nm are shown. For this research is chosen to take 5 as the real refractive index of Pt as the work from [40] is verified with two different models. The imaginary component of the refractive index is chosen to be 15. By choosing a high absorption, a conservative assumption regarding the absorption is made such that the performance of the sensor cannot be overestimated.

<b>Experimental</b>	2+17i [41]
<b>Simulation</b>	6+11.5i [41]
	5.2+7.1i [40]

Table 2.1: Different refractive indices for Pt.

## 2.3. Optical Cavity Sensors

Optical cavity sensors work by coupling light into a cavity and measuring with photodiodes the light intensity that either gets reflected (R) or transmitted (T) out of the cavity, figure 2.3. These measurements are used to determine at what wavelength the cavity is resonating ( $\lambda_{res}$ ) which is a function of the refractive index of the used materials and the geometry of the cavity [42],

$$\lambda_{res} = \frac{Ln_{eff}}{m}. \quad (2.4)$$

Here  $L$  is the round-trip optical path length,  $n_{eff}$  the effective refractive index of the cavity and  $m = 1, 2, 3, \dots$ . The optical cavity can be used as a sensor by deliberately changing either or both the geometry and/or refractive index which in turn shifts  $\lambda_{res}$  and can be measured in the transmission and/or reflection.

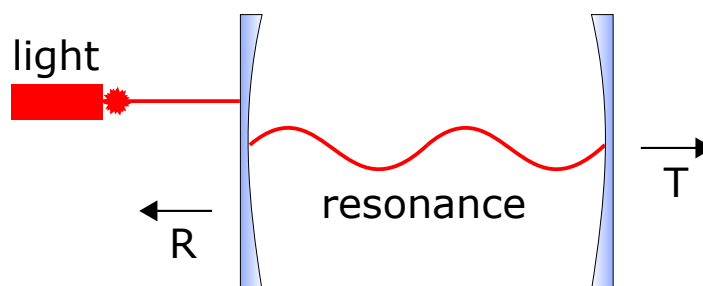


Figure 2.3: An optical cavity consisting of two parallel mirrors where light is coupled in on the left and starts resonating, creating standing waves. These waves can be measured in the light intensity that exits the optical cavity in either the reflection (R) or transmission (T) on the left and right respectively.

An optical cavity resonates because it consists of two highly reflecting mirrors facing each other where

light with certain wavelengths form standing waves known as cavity modes. A standing wave is where two waves with equal frequency moving in opposite directions interfere constructively with each other such that their amplitudes add up. The resulting wave is stationary with an amplitude as high the two separate waves combined. Because in the cavity the light reflects back and forth multiple times, the waves keep on adding up such that the resulting cavity mode has an amplitude much higher than the light that is put in the cavity. Equation (2.4) also shows that if either the length between the mirrors ( $L$ ) or the refractive index of the materials used ( $n_{\text{eff}}$ ) are changed, the standing wave will have a different wavelength.

By coupling light with a variable wavelength in the cavity (i.e. a tuneable laser source), at resonance, the measured reflection and transmittance show either a peak or dip in output indicating that at that specific frequency the cavity is resonating. Figure 2.4 shows such a normalized transmission measurement where there is a peak in the measurement at resonance,  $\lambda_{\text{res}}$ . Cavity modes can be given in either frequency [Hz] or wavelength [m] which are inversely proportional with each other with the speed of light as a constant and are quantified by their quality factor (Q factor). The Q factor is what describes the optical energy loss of a cavity mode where a high Q factor means low optical loss and can be formulated as a function of  $\lambda_{\text{res}}$  and  $\delta\lambda$  (the width of the peak at half the maximal or minimal value) and has no units [43]

$$Q = 2\pi \frac{\text{stored energy}}{\text{dissipated energy per oscillation cycle}} = \frac{\lambda_{\text{res}}}{\delta\lambda}. \quad (2.5)$$

In the transmission measurement of figure 2.4 such a high and low Q factor cavity mode is shown. There is optical energy loss in the cavity because there is absorption and scattering. Absorption occurs due to material properties as light intensity decreases as it travels through a material. Scattering losses is where the light gets refracted into unwanted directions. A mirror surface can for example not be perfectly shaped, or light can pass through the mirror instead of reflect. In both cases, light energy is lost.

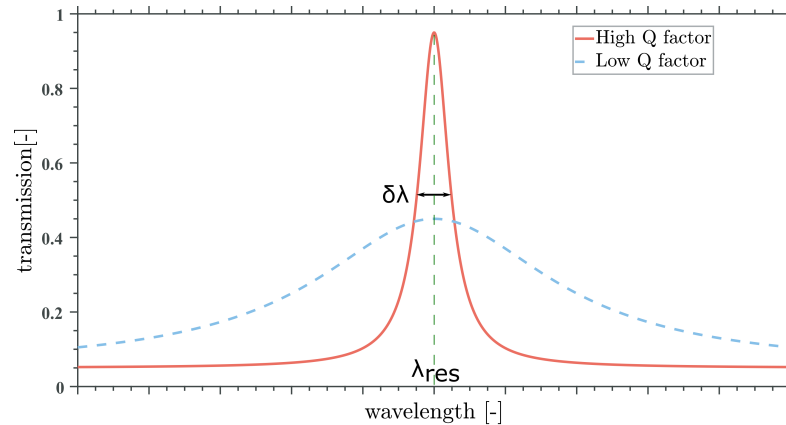


Figure 2.4: The normalized transmission of an optical cavity sensor showing a high and low Q factor cavity mode measurement where  $\lambda_{\text{res}}$  indicates the cavity mode wavelength and  $\delta\lambda$  the linewidth of the Q factor which is inversely proportional to the Q factor given in equation (2.5).

When the Q factor is high, there is little optical loss and light resonates back and forth in the cavity for a long time. Because of this, the light interacts as much as possible with the material such that any change in refractive index of the material will have a bigger effect on the cavity. This makes the cavity a more sensitive sensor which becomes clear later in this section. Next to that, when the Q factor is high, the transmission or reflection measurement shows more clearly at what wavelength the cavity is resonating. The sharpness of the curve makes that a small deviation in wavelength of the input light leads to a large change in measured light intensity such that the exact location can be determined more precise. Finally, a high peak means that there is more contrast in the light intensity at  $\lambda_{\text{res}}$  with respect to the noise-floor that is in the signal. Both the minimum as maximum in the transmission and reflection measurement will in practice never be 0 or 1 as there are always some absorption and scattering losses meaning that some of the light is not transmitted and/or reflected. Important to note is that depending on how the light is coupled in the cavity and where the exiting light intensity is measured (either the reflected or transmitted light), there is either a peak or dip in light intensity at  $\lambda_{\text{res}}$ . This means that either the reflection or transmission can be used to find  $\lambda_{\text{res}}$  as they

are each others inverse.

The cavity modes that occur in the optical cavity are a function of the geometry of the cavity and the refractive indices of the materials that make up the cavity as shown in equation (2.4). That means that if either the cavity geometry or refractive index is changed, the wavelength and amplitude of the cavity mode change with it. Therefore by deliberately changing either or both the geometry and/or refractive index, the cavity can be used as a sensor. Figure 2.5 shows the initial transmission measurement before and after  $H_2$  is added to the cavity (the refractive index has changed). The shift in wavelength that the mode experiences is given with  $\Delta\lambda$ .

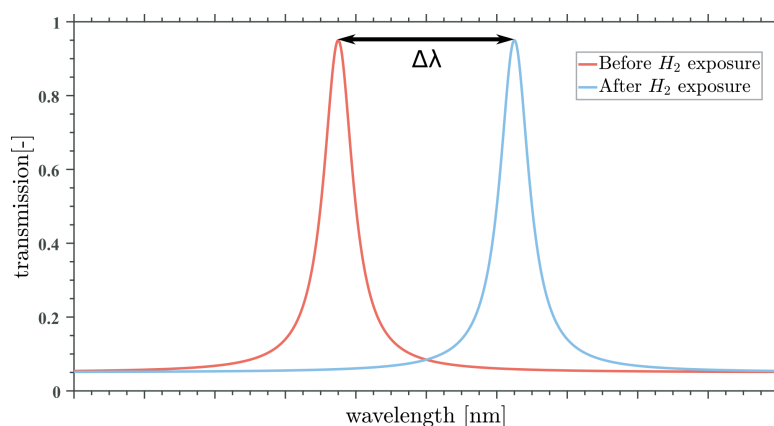


Figure 2.5: The normalized transmission measurement of an optical cavity sensor before (red) and after (blue)  $H_2$  gas is added to the cavity changing in the refractive index where the shift in wavelength is given with  $\Delta\lambda$ .

Optical cavities that measure as a function of the change in geometry are called opto-mechanical cavities and often measure quantities like displacement [44–46], stress [47, 48], magnetic [49] and electric [50] fields because they couple to the mechanical displacement of the cavity in some form. The type of sensors that measure as a function of the refractive index are called resonant refractive index sensors [51]. Optical cavities are often made from semiconductors like Si and are in a gaseous or liquid environment where both the refractive indices of the semiconductor as the surrounding medium define the cavity modes. As a new gas or liquid is introduced in the surrounding medium with a different refractive index, the cavity modes change and a gas or liquid sensor is built. Resonant refractive index sensors can also be used to measure solid particles as a particle can be introduced in the gas or liquid in the cavity, changing the refractive index of the cavity as well. The resulting  $\Delta\lambda$  from this change in refractive index can then be related to the addition of this other material [51–54].

Another type of resonant refractive index sensor is where the material itself, that makes up the cavity, changes refractive index. This means that the change of refractive index does not take place in the gas or liquid but in the solid materials that the cavity is built from. For this, (parts of) the materials that make up the cavity should have a variable refractive index as a function of the quantity that wants to be measured. In this research, the quantity to measure is  $H_2$ . Si is not sensitive towards  $H_2$  exposure which is why an extra material to build up the cavity is used which is sensitive towards  $H_2$  exposure. The refractive index of this material changes when in contact with  $H_2$  which then changes the cavity mode wavelength.

### 2.3.1. Photonic Crystal Nanobeams

Now that the general concept of how an optical cavity sensor, specifically a resonant refractive index sensor works is explained, in this section, a more in-depth understanding of the optical cavity used in this research is given, a PhC nanobeam. A PhC nanobeam is a nanoscale optical cavity in the shape of a beam, figure 2.6. As the figure shows, on both ends of the nanobeam are the mirror sections that reflect the light back and forth inside what is referred to as the defect region. The highly reflective behaviour of the mirror sections comes from the usage of a PhC which is a subwavelength scale periodic arrangement of different refractive index materials which in the case of figure 2.6 is silicon (Si) with a refractive index of 3.4 and the air-filled holes have a refractive index of 1. The periodic change of refractive index in a PhC results in the reflection of

specific wavelengths of light that are incident on the PhC which works as following. When light propagates through the PhC, at each layer interface the light gets partially reflected. Because this happens periodically, these multiple reflections interfere destructively with the incident wave such that the forward-propagating wave is eliminated but the reflected wave isn't. [30]

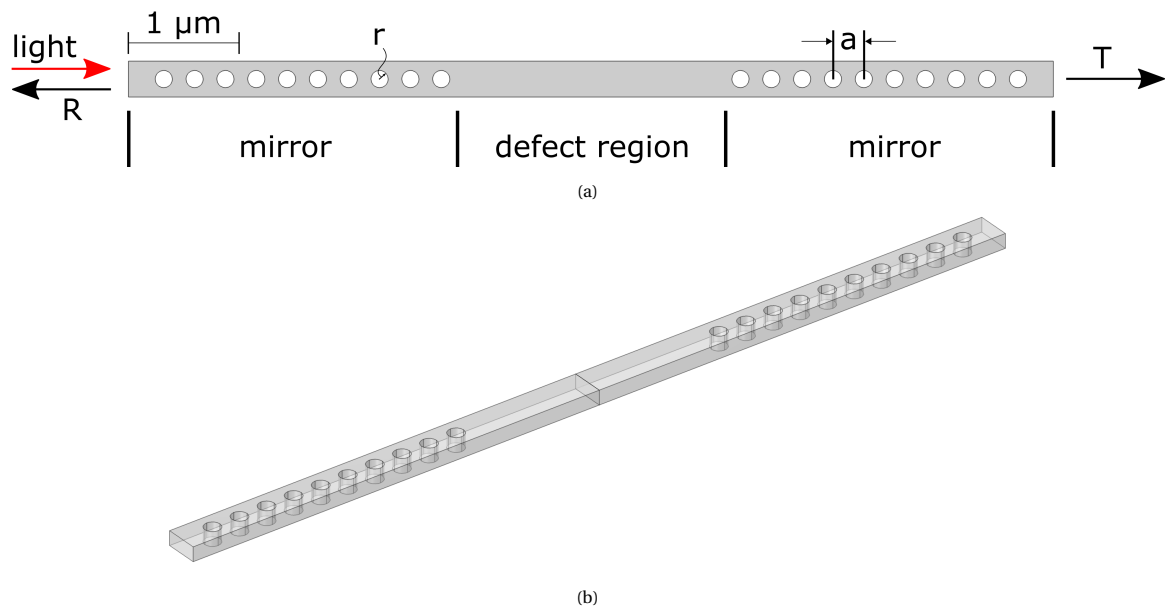


Figure 2.6: The (a) top and (b) 3D view of a PhC nanobeam cavity made from Si.

The periodic structure of a PhC is also referred to as the lattice and the spacing of each segment is called the pitch ( $a$ ). The pitch in figure 2.6 is 430 nm resulting in a cavity mode with a wavelength of approximately 1500 nm. Figure 2.7 shows this cavity mode as the absolute light intensity is plotted in the nanobeam where the red colour represent high light intensity and the blue colour low. The figure shows that the high light intensity is situated in the high refractive index region which is typical for a PhC.

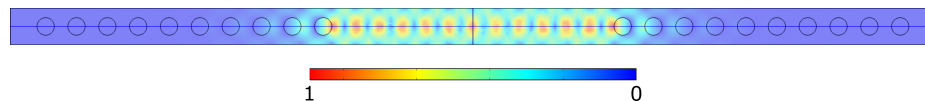


Figure 2.7: Top view of a cavity mode in a PhC nanobeam cavity.

Using a PhC nanobeam as the optical cavity has multiple advantages. Si has low optical absorption at telecom wavelengths (1500 nm) and is easy to fabricate on micrometre scales. Because of this, the cavity can easily be integrated in for example a system-on-a-chip. Next to that, because of the physics in the nanobeam, there are no alignment issues with placing the two mirrors parallel with each other which is something you could expect if two separate mirrors have to be aligned like in figure 2.3 [42, 55]. The defect region in figure 2.6 is a solid piece of Si wherein the cavity mode is located as seen in figure 2.7. A common improvement to optimize this defect region is by adding holes in this region as well, figure 2.8a [53, 56–60]. Here the hole radii and pitch have a decreasing taper towards the centre of the cavity which confines the light more to the centre and simultaneously increases the reflectivity of the PhC. As mentioned in section 2.3, part of the optical loss in a cavity is scattering losses where light is reflected in unwanted directions. As the light in the defect region propagates through the silicon, the tapered holes make sure that these scatter losses from the sudden shift in refractive index are more smooth, increasing the Q factor of the cavity by several orders of magnitude [42, 61]. The resulting cavity mode from the improved design can be seen in figure 2.8b where the Q factor is almost 1 million compared to a Q factor of 3000 for the not improved design from figure 2.7. As mentioned in section 2.3 as well, the high Q factor is desired to accurately find the resonance wavelength of a cavity mode. Next to that, with a high Q factor, light reflects more often back and forth in the cavity such that there is more light-matter interaction making the sensor more sensitive for a change in the material. Also, as the light is more

confined in the defect region, only in that small area of the nanobeam the change in refractive index is important. That means that if for example a small particle is introduced in the defect region, almost all of the light is affected by this. If the mode would be more spread out, more particles needed to be introduced to create the same change in the cavity mode. This all shows how important a high Q factor is for the performance of the sensor. Apart from the Q factor there are other quantities that determine the performance of the H<sub>2</sub> sensor in this research. In the next section, these performance measures are given.

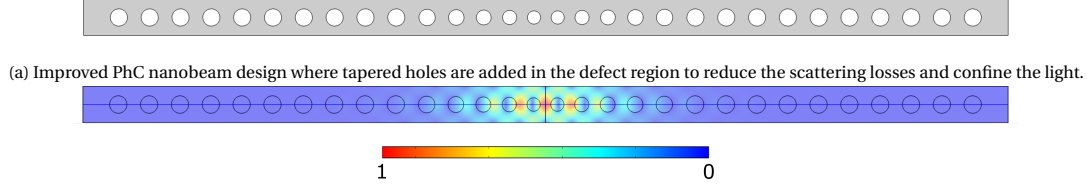


Figure 2.8: The top view of (a) the improved PhC nanobeam design and (b) its corresponding cavity mode.

### 2.3.2. Sensor Performance

The performance targets that are of interest for this sensor are the minimum detectable concentration of 0.1% H<sub>2</sub> and the response time of < 1 second. Both these performance targets are dependent of each other which will be made clear in section 3.2. First in this section, how each performance target is obtained is given.

#### Figure of Merit

Starting with the measurement range, a high Q factor is desired because the higher the Q factor is, the more exact the resonance wavelength can be determined. Next to that, not only a high Q factor is important but also a high sensitivity (S). The sensitivity shows how much the resonance wavelength of a mode changes ( $\Delta\lambda$  in figure 2.5) per change of refractive index of the cavity material,

$$S = \frac{\Delta\lambda}{\Delta n}. \quad (2.6)$$

The sensitivity is often given in  $\frac{nm}{RIU}$  where RIU stands for refractive index unit which translates to how much the wavelength of a cavity mode shifts (in nm) for a change in refractive index of 1 (e.g.  $n=2 \rightarrow n=3$ ) [29, 51, 52, 54, 62]. This means that when a material changes a little in refractive index and the mode shifts are large amount in wavelength, the sensitivity is high.

Both the Q factor and sensitivity need to be high for the sensor to measure these small concentrations of H<sub>2</sub> which is illustrated in figure 2.9. The first two plots as seen from the legend correspond with a transmission measurement when 0% and when 100% H<sub>2</sub> is added to the sensor where both the Q factor and sensitivity are high. This means that both peaks are narrow, high in amplitude and far apart. The two other plots in the figure also show how a mode changes if the concentration goes from 0% to 100%, however here the Q factor and sensitivity are lower. In this case, determining  $\lambda_{res}$  and following the mode as it moves when H<sub>2</sub> is added is harder which overall reduces the ability to measure low concentrations.

It is the combination of both the Q factor and the sensitivity that determines the overall performance regarding the measurement range. Therefore, in order to compare different designs with each other by simplifying the performance quantity of a sensor, a figure of merit is defined [54, 63, 64],

$$FOM = \frac{SQ}{\lambda_{res}} = \frac{\Delta\lambda}{\Delta n \delta\lambda}. \quad (2.7)$$

This figure of merit increases as both the Q factor and the sensitivity increase and can be determined theoretically through simulations and literature research. As practically all resonant refractive index sensors in literature are at least defined by their Q factor and sensitivity, this figure of merit is a good way to compare with these other sensors.

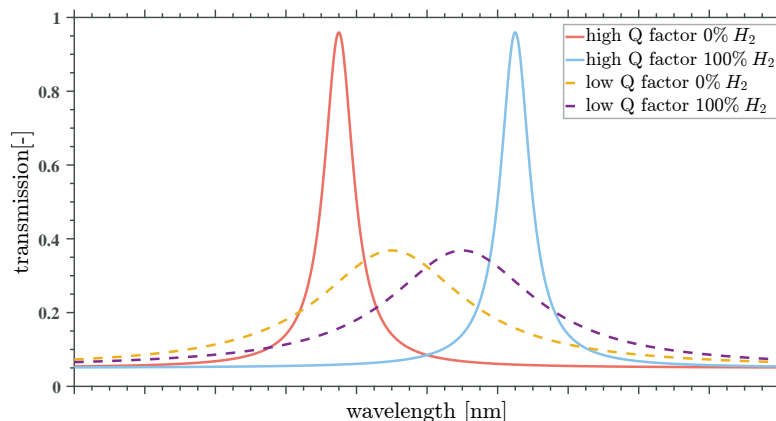


Figure 2.9: There are two sets of modes (red+blue and yellow+purple) where the first set of modes show what high sensitivity and high Q factor looks like in a transmission plot and the second set of modes show how for a lower sensitivity and Q factor it is harder to measure a clear difference between the modes.

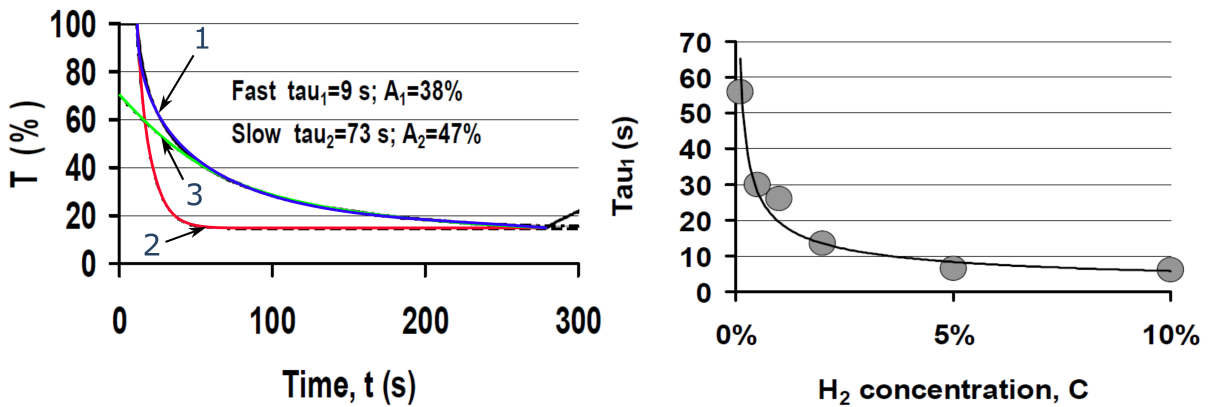
## 2.4. Reaction Times

Next to being able to measure low enough concentrations of  $H_2$ , the time in which the sensor measures these concentrations is the second performance target that is important for this research. A common variable to determine this reaction times is the time it takes for the sensor to reach 90% of its final value,  $t_{90}$ . As explained in section 2.1, the chemical reaction between  $WO_3$  and  $H_2$  is what changes the refractive index in the sensor which is the measuring principle of this  $H_2$  sensor. This reaction is rather slow compared to the 1 second performance target as for low concentration of  $H_2$  it can quite quickly take minutes for the reaction to occur and is a bottleneck for many  $H_2$  sensors as mentioned in the introduction. In this thesis, no experiments on the reaction time of  $WO_3$  have been performed which is why a literature review on these reaction times is done to find the limitations that are imposed by this chemical reaction regarding the overall performance of the sensor. The reaction time is dependent on multiple factors like growth and substrate temperatures, deposition rates, crystallinity, reaction temperature, film thickness and catalyst [6, 7, 11]. In this section, the focus is put on the layer thicknesses of the  $WO_3$  and Pt at which a layer setup is derived which in theory meets the performance target. Each paper measures the transmittance ( $T$ ) of a certain sample as a function of  $H_2$  exposure. The assumption is made that the refractive index of  $WO_3$  changes simultaneously with its transmittance so that these results can be used to obtain information about the refractive index of  $WO_3$ .

Hoagland et al. [37] have done measurements on the reaction times of a 500 nm thick  $WO_3$  film with 3 nm thick Pt film on top when exposed to a concentration of  $H_2$  by measuring the relative transmittance ( $T$ ) as a function of the time ( $t$ ). In figure 2.10a,  $T(t)$  is plotted when the sample is exposed to a 0.5%  $H_2:N_2$  mixture where line 1 (blue) represents the actual measured  $T(t)$ , showing that it takes about 200-300 seconds for the reaction to fully occur. They then approximate the measurement (line 1) with an equation to find that it is best described with a fast and slow exponential function, line 2 (red) and 3 (green) respectively,

$$T(t) = T_0 + A_1 \exp\left(\frac{t_0 - t}{\tau_1}\right) + A_2 \exp\left(\frac{t_0 - t}{\tau_2}\right). \quad (2.8)$$

For this equation,  $\tau$  represents the time it takes for the transmittance to change by  $1/e$  of the total maximum change in transmittance. They argue that the reaction consists of a fast and slow component because after the  $H_2$  has been dissociated by the Pt, a part of the H atoms diffuse through the Pt in the  $WO_3$  and another part diffuses over the Pt to the edge of the sample where the  $WO_3$  is not covered with Pt. Which component is slow or fast is not mentioned but the assumption is made that the reaction where the H atoms have to diffuse through the Pt is the slow reaction. From this is concluded that the reaction occurs quicker when some  $WO_3$  is not covered in Pt so that the H atoms don't have to diffuse through the Pt.



(a) The relative transmittance ( $T$ ), as function of time for a  $500 + 3$  nm thick  $\text{WO}_3$  Pt film when exposed to a 0.5%  $\text{H}_2:\text{N}_2$  mixture line 1 (blue). The response a function of the  $\text{H}_2$  concentration ( $C$ ) approximated by equation (2.9). The is approximated with a fast and slow exponential function, line 2 (red) and 3 name  $\tau_1$  in this figure doesn't correspond to the time constant of line 2 in figure 2.10a but to the time constant of line 1.

Figure 2.10

In figure 2.10b, the time constant is given as a function of the  $\text{H}_2$  concentration,  $C$  and approximated with

$$\tau = 1.7122C^{-0.5271} \tag{2.9}$$

The figure says  $\tau_1$  but when filling in  $C=0.005$  (which corresponds to 0.5%) it gives  $\tau_1 = 28\text{s}$  instead of  $\tau_1 = 9\text{s}$  which indicates that this is the time constant for the whole reaction and not either the fast or slow component. This figure clearly shows the exponential relation between the reaction time and the  $\text{H}_2$  concentration that as the concentration goes below about 2%, the reaction time increases significantly.

Interestingly, they have also measured  $T(t)$  for a  $\text{WO}_3 + \text{Pt}$  powder mixture when it is exposed to 0.5%  $\text{H}_2$ , figure 2.11. They have derived the time constant of the response to be 0.78 seconds which is significantly faster compared to 28 seconds. This has likely to do with that in the powder there are more spots where the  $\text{WO}_3$  is not covered with Pt so that the H atoms can diffuse more easily in the  $\text{WO}_3$ . This again shows that for a fast reaction it can be beneficial to have some  $\text{WO}_3$  not covered in Pt so that the H atoms don't have to diffuse through the Pt.

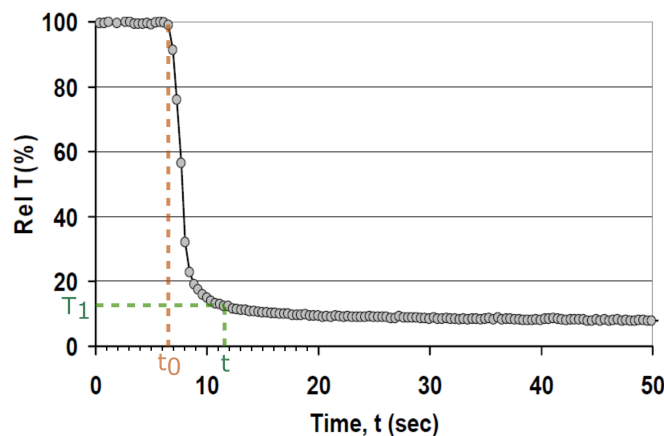


Figure 2.11: The change in relative transmittance of a  $\text{WO}_3 + \text{Pt}$  powder versus the time from Hoagland et al. [37].

Hsu et al. [21] has experimented with 400 nm thick  $\text{WO}_3$  thin films with Pt nanoparticles deposited on top showing a  $t_{90} = 5\text{s}$  for 0.5%  $\text{H}_2$  in carrier gas  $\text{N}_2$ . The Pt nanoparticles correspond with a layer thickness of about 2.5 nm. Chen et al. [65] measures the transmittance change in a 500 nm thick  $\text{WO}_3:\text{Pd}$  mixture with a volume ratio of  $\text{Pd} : \text{WO}_3 = 1 : 150$ . Here they are measuring  $t_{90} = 13\text{s}$  for 4% of  $\text{H}_2$  and  $t_{90}$  is approximately one minute when the concentration goes down to 0.5%. Chan et al. [66] has done numerous experiments on

different thickness  $\text{WO}_3$  Pt thin films showing that the best results are obtained for 700 nm thick  $\text{WO}_3$  layer with on top 15 nm of Pt, figure 2.12. Here is clearly visible how even for 1%  $\text{H}_2$  the slope is rather steep estimating  $t_{90}$  to be about 10 to 15 seconds.

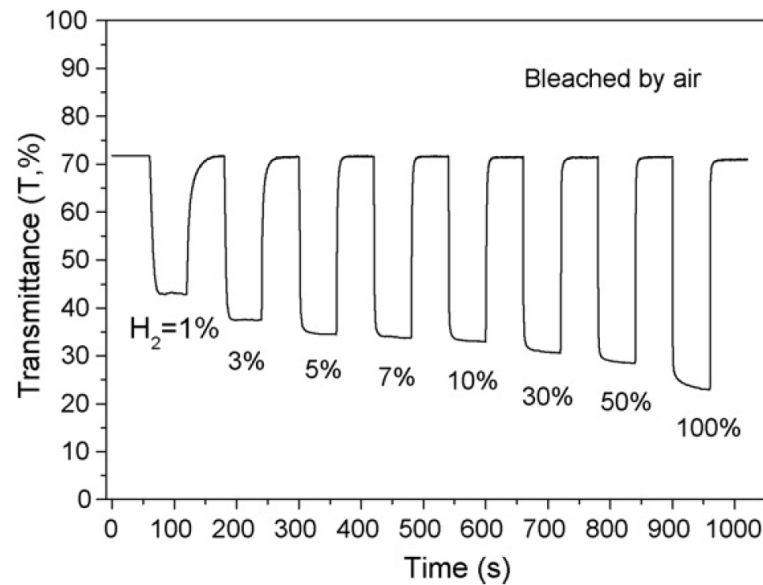


Figure 2.12: The change in relative transmittance of a  $\text{WO}_3 + \text{Pt}$  powder versus the time from France et al., ref. [37].

Zhuang et al. [31] fabricated a 200 nm thick  $\text{WO}_3$  and Pd film via the sol-gel method and measured the film transmission as a function of the time when applying a 5%  $\text{H}_2$ :Ar mixture, figure 2.13. For the sol-gel method the catalyst is uniformly distributed through the  $\text{WO}_3$ . The figure shows a significant decrease in reaction time as the Pd:W mol ratio goes from 1:125 to 1:40 with for the latter ratio a  $t_{90}$  of about 40 seconds.  $\text{WO}_3$  is more than 3 times as large as Pd in volume leading to a volume ratio of about 1:120 instead of 1:40.

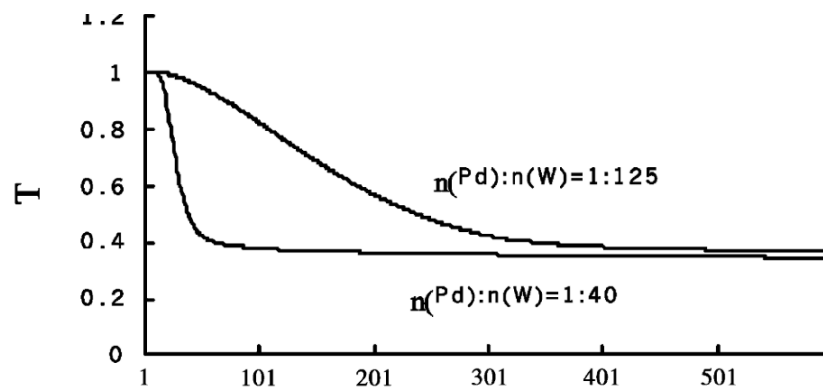


Figure 2.13: Reaction times for two different Pd:W ratios [31].

In order to get an overview of the different findings and derive further conclusions from them, they are summarized in table 2.2. The measurements by Hoagland et al. [37] indicate that the reaction time increases significantly if the H atoms have to diffuse through the catalyst to reach the  $\text{WO}_3$ . By using Pt nanoparticles instead of a uniform layer of Pt there is bare  $\text{WO}_3$  such that the H doesn't have to diffuse through the Pt that much. This is also confirmed by the measurements done by Hsu et al. [21] because they show the fastest reacting times from table 2.2 and are the only setup that uses nanoparticles. A layer of nanoparticles has more surface area per volume than a uniform layer resulting in more surface area for the reaction to occur. From this can also be derived that it would be better to have a large number of small nanoparticles compared

to a small number of large nanoparticles to increase the surface to volume ratio as much as possible. For a fast reaction time, the assumption is made that the  $\text{WO}_3$  layer needs to be thin and there should be a large amount of catalyst present in the form of nanoparticles.

Table 2.2: Reaction times of  $\text{WO}_3$  with Pd or Pt sensors/thin films.

Literature	$\text{WO}_3$ + Catalyst Layers	Catalyst: $\text{WO}_3$ Volume ratio	$t_{90}$ [s]
Hoagland et al. [37]	500 + 3 Pt	1:167	100 for 0.5% $\text{H}_2$
Hsu et al. [21]	400 + Pt nanoparticles on top	1:150	5 for 0.5% $\text{H}_2$
Chen et al. [65]	500 $\text{WO}_3$ Pd mixture	1:150	60 for 0.5% $\text{H}_2$
Chan et al. [66]	700 + 15 Pt	1:47	15 for 1% $\text{H}_2$
Zhuang et al. [31]	200 $\text{WO}_3$ Pd mixture	1:120	40 for 5% $\text{H}_2$

Because none of the literature meets the 1 second performance target, the best performing literature (Hsu et al. [21]) is taken and from there a layer thickness is derived which does meet this target. Their setup consists of a 400 nm thick  $\text{WO}_3$  layer with Pt nanoparticles on top and reacted within 5 seconds to 0.5%  $\text{H}_2$ . Making a conservative assumption that the reaction times decreases linearly with the  $\text{WO}_3$  layer thickness means that an 80 nm thick layer would react within 1 second with 0.5%  $\text{H}_2$  which almost meets the reaction time performance target of 1 second for 0.1%  $\text{H}_2$ . Regarding the Pt, it is a collection of nanoparticles shaped as a hemisphere. In the paper from Hsu et al. [21], the volume of the nanoparticles, as if they were melted and spread out, corresponds to a 2.5 nm thick layer of Pt. Because nothing else is documented about the nanoparticles, from now on is assumed that the nanoparticles have a radius of 3 nm. By having such a small radius, the surface to volume ratio is large which has shown to be favourable for a fast reaction time. To quantify the nanoparticles for further use in the research, the density (the amount of particles per surface) is obtained which is for the 2.5 nm thick Pt layer,  $4.4 \cdot 10^4$  particles/ $\mu\text{m}^2$ . As the  $\text{WO}_3$  layer thickness goes from 400 nm to 80 nm, two assumptions regarding the density can be made: The density is not dependent on the  $\text{WO}_3$  layer thickness or the density is dependent on the  $\text{WO}_3$  layer thickness. For the first assumption, as the  $\text{WO}_3$  layer thickness decreases, the surface at which the  $\text{H}_2$  reacts stays the same thus the density of nanoparticles stays  $4.4 \cdot 10^4$  particles/ $\mu\text{m}^2$ . On the other hand, with a lesser volume of  $\text{WO}_3$ , less  $\text{H}_2$  has to be dissociated which in turn requires less Pt for the reaction resulting in  $8.8 \cdot 10^3$  particles/ $\mu\text{m}^2$ . Pt has due to its high absorption a large effect on the performance on the sensor which is why the performance as a function of nanoparticle density is simulated.



# 3

## Methods

In this chapter is explained how the simulations and optimizations are done. Next to that, the initial sensor design is given and a flow on how the performance of the sensor is analyzed is explained.

### 3.1. Simulation

To simulate and optimize the sensor, MathWorks® MATLAB and finite element software COMSOL Multi-physics® is used. With the wave optics module in COMSOL, the physics of the electromagnetic waves in the sensor is simulated by solving Maxwell's equations and performing an eigenfrequency analysis to study the resonances of the cavity. The eigenfrequency analysis shows at what frequency there is a cavity mode, how the light intensity is distributed across the geometry and what the Q factor is of this cavity mode as a function of for example, the refractive index. The simulations are controlled from MATLAB such that multiple simulations with different parameters are automated and that optimization algorithms from MATLAB can be integrated.

The typical simulation mesh of half a PhC nanobeam with two extra layers ( $\text{WO}_3$  and Pt) on top is shown in figure 3.1a. Only half the nanobeam has to be simulated because of its symmetry around the defect region. Around the nanobeam there is a large cylinder representing air with a radius of multiple wavelengths large. The radius is large so that the boundaries of the domain (yellow) do not cause any unwanted interference when solving the model. This boundary is referred to as the scattering boundary condition and mimics as if the nanobeam is suspended in an open environment where the boundaries are infinitely far away. The red boundary on the left flat side of the cylinder is a perfect magnetic boundary condition which is there to mirror the physics because only the right-half nanobeam is simulated.

#### 3.1.1. Optimization

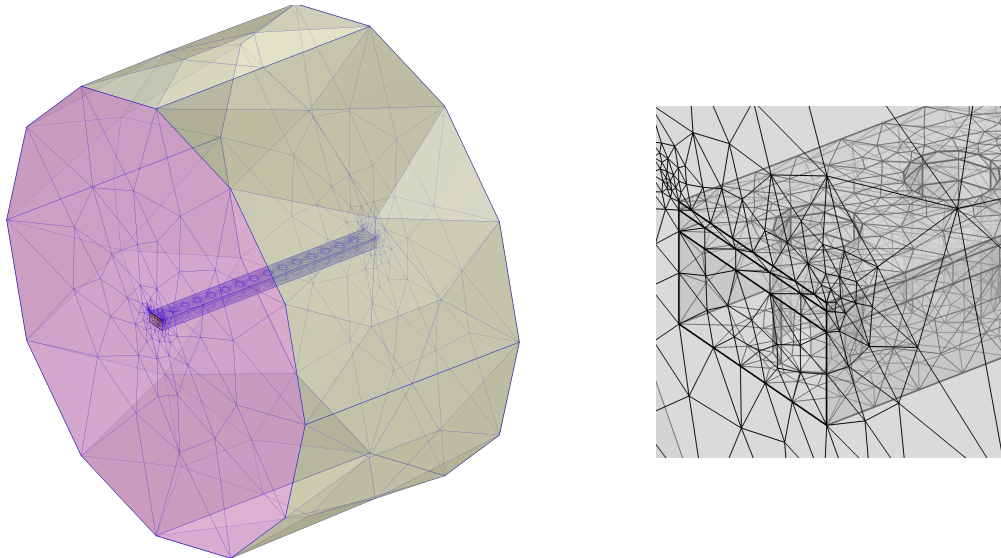
To get a better idea of what performance can be expected of a specific design, an optimization for the Q factor is done where the geometry of the design is altered to find better optical modes. Table 3.1 shows each parameter of the optimization and its initial value. As mentioned in the background, section 2.3.1 and shown in figure 2.6a, the nanobeam consists of a mirror and defect region. The hole sizes and distances in the defect region are tapered such that the Q factor is high. In the optimization, the spacing, x and y radii in this defect region are specified with a quadratic taper such that each part is described by three parameters leading to 9 parameters. The spacing, x and y radius in the mirror are constant and thus described with constants resulting in a total of 12 parameters that can be divided into 4 types.

```

Nmax = 15;
Ncav = 5;
hole_pos = 330e-9/2;

for i = 0:Nmax-1
    if i == 0
        prev_hole_pos = hole_pos;
        hole_rx = min_hole_x;
        hole_ry = min_hole_y;
    elseif (i > 0) && (i < Ncav)
        hole_pos = prev_hole_pos + min_hole_a * (1 + c_a_1 * prev_hole_pos + c_a_2 * ...
            prev_hole_pos.^2);
        hole_rx = min_hole_x * (1 + c_x_1 * hole_pos + c_x_2 * hole_pos.^2);
        hole_ry = min_hole_y * (1 + c_y_1 * hole_pos + c_y_2 * hole_pos.^2);
    else
        prev_hole_pos = hole_pos;
        hole_pos = prev_hole_pos + mirr_a;
        hole_rx = mirr_x;
        hole_ry = mirr_y;
    end
    prev_hole_pos = hole_pos;
end
end

```



(a) A typical mesh for a PhC nanobeam with two extra layers ( $\text{WO}_3$  and Pt) on top where the yellow indicates a scattering boundary condition and the red a perfect magnetic conductor boundary condition. (b) A zoom in of the mesh illustrating how the curvature of the holes is approximated with the mesh and how the mesh is finer for the solid materials opposed to the air region around it.

Figure 3.1

The optimization is done in MATLAB with the `fminsearch` algorithm that uses the Nelder-Mead Method to find the local minimum of an unconstrained multivariable nonlinear function without the use of derivatives and it is a gradient optimizer [67]. The MATLAB algorithm simulates the nanobeam in COMSOL with a certain Q factor as the output, it then changes a parameter, simulates again and based on that decides which parameters change is the right one. The assumption is made that the initial design is optimized, that means that adding a  $\text{WO}_3$  layer to that design shall create a new design which is slightly offset from that optimum and with that assumption the solution space should be convex which means that this optimizer will find the new optimum for this slightly altered design. Two different nanobeam designs are optimized, each design starts with the same set of initial parameters and has a 20 nm thick  $\text{WO}_3$  layer on top. For the first design, the imaginary refractive index of the  $\text{WO}_3$  layer is low ( $1 \cdot 10^{-6}$ ) representing a  $\text{H}_2$  sensors without Pt and for the other design the imaginary refractive index is high (0.01) representing the  $\text{H}_2$  sensor with Pt. The choice is made not to simulate the Pt nanoparticles but to increase the absorption in the  $\text{WO}_3$  layer because simulation all the nanoparticles is computationally not possible with the available computational power. Both optimizations are done to see whether a high or low imaginary refractive index pushes the optimization to a

higher Q factor more easily. Figure 3.2 shows the Q factor versus the imaginary refractive index of the WO<sub>3</sub> to give an idea of how the Q factor decreases.

Table 3.1: The initial optimization parameters derived from the initial nanobeam geometry taken from Deotare et al. [60].

Type	Parameter	Meaning	Value
Defect region hole spacing	min_hole_a	Minimal hole spacing	$330.0 \cdot 10^{-9}$ m
	c_a_1	Linear scaling of hole spacing	$0.1870$ m <sup>-1</sup>
	c_a_2	Quadratic scaling of hole spacing	$0$ m <sup>-2</sup>
Defect region hole x radius	min_hole_x	Minimal hole x radius	$92.40 \cdot 10^{-9}$ m
	c_x_1	Linear scaling of x radius	$0.1450$ m <sup>-1</sup>
	c_x_2	Quadratic scaling of x radius	$0$ m <sup>-2</sup>
Defect region hole y radius	min_hole_y	Minimal hole y radius	$92.40 \cdot 10^{-9}$ m
	c_y_1	Linear scaling of y radius	$0.1450$ m <sup>-1</sup>
	c_y_2	Quadratic scaling of y radius	$0$ m <sup>-2</sup>
Mirror	mirr_a	Mirror spacing	$430.0 \cdot 10^{-9}$ m
	mirr_x	Mirror x radius	$120.4 \cdot 10^{-9}$ m
	mirr_y	Mirror y radius	$120.4 \cdot 10^{-9}$ m

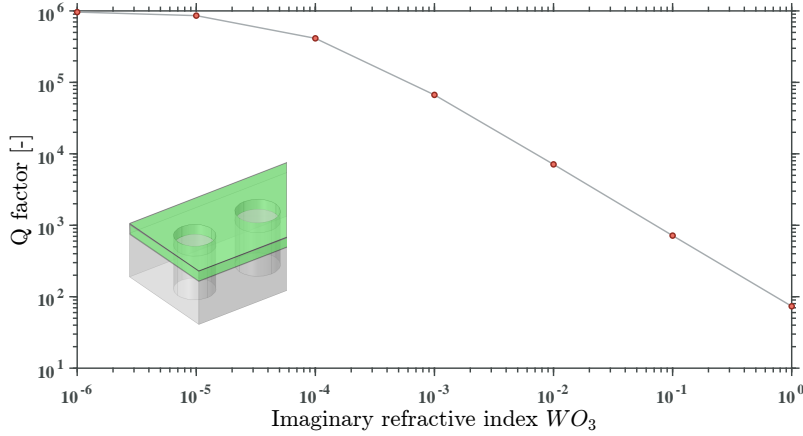


Figure 3.2: The imaginary refractive index of the 20 nm WO<sub>3</sub> layer versus the Q factor.

### 3.2. Initial H<sub>2</sub> Sensor Design

In order to make a PhC nanobeam H<sub>2</sub> sensor, first an initial Si nanobeam design needs to be decided on which can then be altered with H<sub>2</sub> sensitive materials to make into a H<sub>2</sub> sensor. In literature there are many Si nanobeam designs with high Q factors [53, 56–60]. What all these designs have in common is that the holes are (almost) circles, the resonance wavelength is around 1500 nm, in the cavity the hole sizes and/or distances are tapered and each design claims Q factors of about 1 million. One of the papers for which the nanobeam geometry is described in most detail is used as the initial design for the sensor, Deotare et al. [60]. Figure 3.3 shows the right-half geometry of the nanobeam. As the nanobeam is symmetric only half the nanobeam is enough to describe its geometry which means that from now on in this research only the right-half geometry is given when a nanobeam is shown. The pitch in the defect region has a six-hole long linear tapering going from 330 nm to 430 nm whereas the remaining 9 holes have a constant pitch of 430 nm. The position of each hole with respect to the previous hole is given with  $p_x$  where  $x$  represents the hole number from left to right

starting with zero and the hole radius is given by  $r$ ,

$$\begin{cases} p_x = 165 & \text{for } x = 0 \\ p_x = p_{x-1} + 330 + 20x & \text{for } 1 \leq x \leq 5 \\ p_x = p_{x-1} + 430 & \text{for } x \geq 6 \end{cases} \quad (3.1)$$

$$r = 0.28a. \quad (3.2)$$

The overall nanobeam with its 30 holes is 13  $\mu\text{m}$  long, 220 nm deep and 500 nm wide. The resulting cavity mode resonates at 1521 nm and has a Q factor of  $9.9 \cdot 10^5$

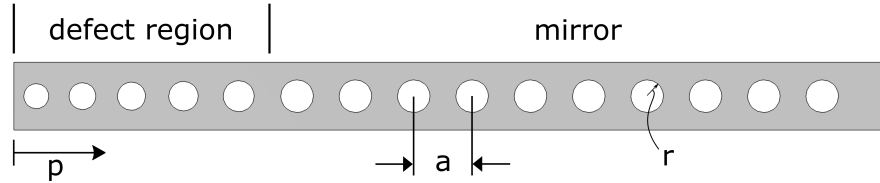


Figure 3.3: The right-half geometry of the initial Si nanobeam design taken from Deotare et al. [60] which will be used to make a  $\text{H}_2$  sensor from.

Now the  $\text{WO}_3$  and Pt are added to the optical cavity such that a  $\text{H}_2$  sensor with a high figure of merit and fast reaction time can be made. The layer thickness of the  $\text{WO}_3$  is limited to about 80 nm as derived in section 2.4. Next to that, a large surface area at which the  $\text{H}_2$  reaction can take place is desired. This means that the  $\text{H}_2$  sensitive materials need to be placed such that the surface to volume ratio is high which is why is chosen to place a layer of  $\text{WO}_3$  on top of the nanobeam with the Pt on top of that, figure 3.4. Important to remember is that there is a constraint on how the layers can be added because of the etching process in nanofabrication where flat layers are added on a chip and then etched according to a pattern. In figure 3.4, the Pt (red) is added as a thin film layer and not as nanoparticles. It is true that in practice, for the best performing sensor, the Pt layer will be a collection of nanoparticles instead of a thin film. However, in this section of the research, first a general overview of how the nanobeam performs when these layers are added is given. This general overview is then used to find the actual performance in the results, chapter 4. Because simulating Pt nanoparticles is very costly and a thin film illustrates the absorption similarly, the choice is made to simulate with a thin film here.

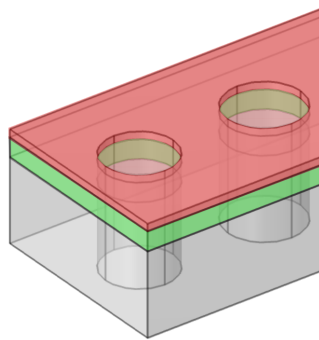


Figure 3.4: The Pt (red),  $\text{WO}_3$  (green) and Si (grey) layers of the sensor from top to bottom respectively.

First a layer of  $\text{WO}_3$  is placed on top of the Si nanobeam to see what the effect of this layer is on the Q factor of the cavity mode. In figure 3.5, the Q factor of a nanobeam with a single layer of  $\text{WO}_3$  versus the layer thickness is shown in red. The blue line will be discussed later. The figure shows that the Q factor decreases as the layer thickness increases which is likely because of two reasons. The  $\text{WO}_3$  and Si both have a different refractive index of 2 and 3.4 respectively. Since the whole concept of a PhC is that the refractive index is periodic where there is ideally a big difference between both refractive indices (1 for air and 3.4 for Si), distorting

this periodicity by adding a layer that has got another refractive index than 3.4 or 1 very likely has a negative effect on the functioning of the PhC, decreasing the Q factor. Next to that, the nanobeam is optimized for a specific geometry, adding a layer in general changes this geometry such that the Q factor is not on its optimal point anymore. To see whether the Q factor decreases because of the different refractive index layer or simply because the geometry is changed, the same simulation is done where the added layer is not made from WO<sub>3</sub> but Si, figure 3.5. For this second simulation, the Q factor doesn't show a particular increase or decrease as the layer thickness increases. This means that it is specifically the refractive index of the added layer that has a negative effect on the workings of the PhC distorting the periodicity of 3.4 and 1.

The two simulations in figure 3.5 aren't smooth lines which is something you would not immediately expect. The non-smooth behaviour of the line can either be because the mesh is not fine enough such that calculation errors due to the large mesh size become significant. To investigate this, the simulation with the added WO<sub>3</sub> layer is done again but with a significantly finer mesh where the computation time of one simulation goes from 4 minutes to 15 minutes as an indication of the increased degrees of freedom from the mesh refinement, figure 3.6. The resulting data is still not smooth which indicates that the mesh is fine enough. The most probable reason for this result is that at certain thicknesses the mode doesn't experience as much scattering as for other thicknesses purely due how the mode propagates through the material and scatters.

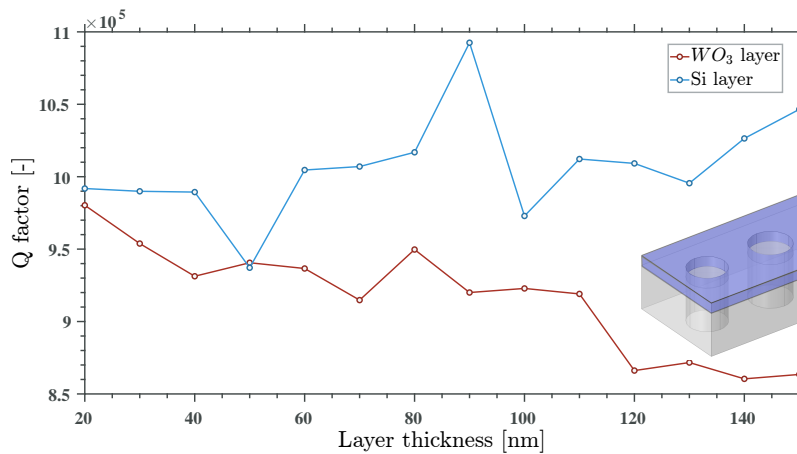


Figure 3.5: The Q factors of a Si (grey) nanobeam with either a WO<sub>3</sub> or extra Si layer on top (the blue layer represents any of the two added layers) versus the WO<sub>3</sub>/Si layer thickness to confirm that the addition of WO<sub>3</sub> specifically is what decreases the Q factor compared to an added Si layer.

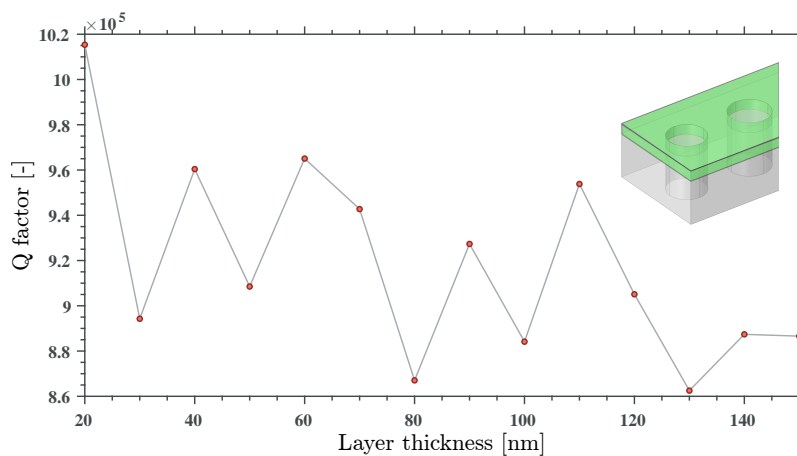


Figure 3.6: The Q factor of a Si (grey) nanobeam with a WO<sub>3</sub> layer (green) on top versus the WO<sub>3</sub> layer thickness where the mesh is finer compared to the simulation in figure 3.5 showing the non-smooth behaviour of the data in figure 3.5 isn't because of a too course mesh but because of different scattering at different thicknesses.

To summarize, the added  $\text{WO}_3$  layer does decrease the Q factor due to its different refractive index but the order of magnitude stays fairly similar. Why the Q factor stays fairly similar is likely because the cavity mode is mostly situated in the Si. In figure 3.7 the cross-sections of a nanobeam with a  $\text{WO}_3$  layer are shown, confirming that indeed the light intensity is mostly in the Si. This means that whatever effect the  $\text{WO}_3$  has on the cavity mode is low.

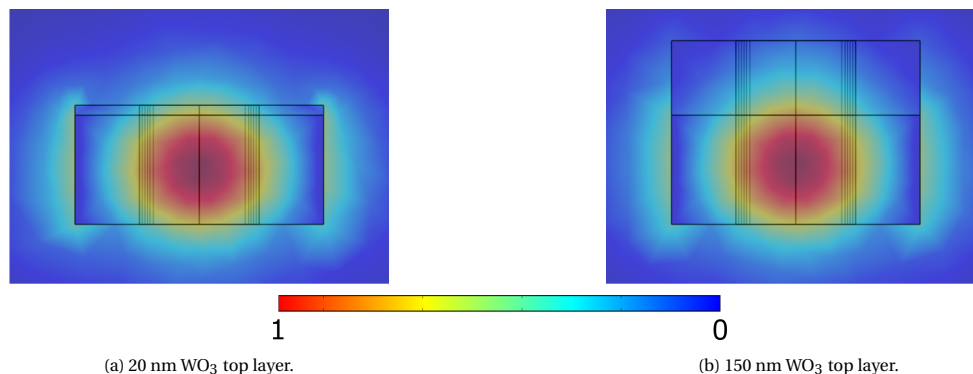


Figure 3.7: The cross-sections of a Si nanobeam with an (a) 20 nm and (b) 150 nm  $\text{WO}_3$  layer on top showing that parts of the light mode that are in the air can be within the  $\text{WO}_3$  which will increase the sensitivity which can also be seen in figure 3.8 where the Q factor is plotted versus the  $\text{WO}_3$  layer thickness.

Next is to investigate what the addition of the  $\text{WO}_3$  layer does to the sensitivity which was how much the cavity mode wavelength changes when the refractive index changes, figure 3.8. This figure clearly shows that as the layer thickness increases, the sensitivity increases with it. This is expected because as the layer becomes thicker, more of the light mode gets situated in the  $\text{WO}_3$ , figure 3.7. This increases the light-matter interaction which is as expected needed for a high sensitivity. The sensitivity increase seems to reach a maximum because the graph is flattening. The flattening is there because at a certain thickness all the part of the light mode which could be in the  $\text{WO}_3$  is in it and increasing the layer thickness doesn't change that anymore.

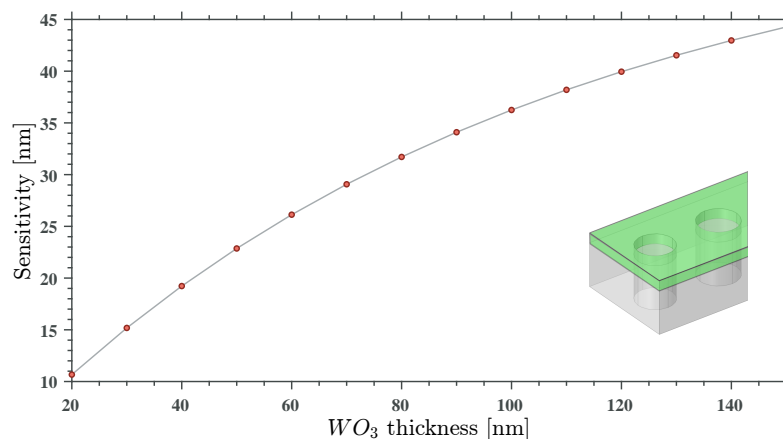


Figure 3.8: The sensitivity of a Si (grey) nanobeam with a  $\text{WO}_3$  layer (green) on top versus the  $\text{WO}_3$  layer thickness showing that the sensitivity increases as expected when more light mode is in the  $\text{WO}_3$  but reaching a maximum because at some point all the light mode which could be in the  $\text{WO}_3$  is in it.

From this can be concluded that the added  $\text{WO}_3$  decreases the Q factor and increases the sensitivity. As both the Q factor and the sensitivity define the figure of merit, in figure 3.9 the figure of merit is plotted versus the  $\text{WO}_3$  layer thickness showing that the increase in sensitivity is dominant over the decrease in Q factor. This means for now that adding a 150 nm thick layer of  $\text{WO}_3$  yields the best result. Increasing this layer above 150 nm could increase the figure of merit even more as the sensitivity has not reached its maximum yet. However, this increase will not be much more as the sensitivity is already rather flat at 150 nm and next to that,

layer thicknesses above 150 nm react too slow with  $H_2$  making it not relevant to investigate.

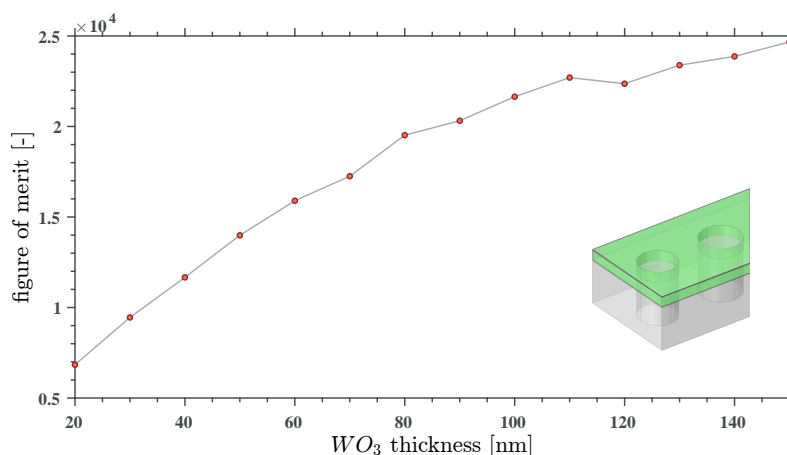


Figure 3.9: The figure of merit of a Si (grey) nanobeam with a  $WO_3$  layer (green) on top versus the  $WO_3$  layer thickness showing that the figure of merit increases as expected as the increase in sensitivity is much larger than the decrease in Q factor for an increasing  $WO_3$  layer thickness.

Not only a layer of  $WO_3$  but also a layer of Pt will be added to the nanobeam as the Pt is there to catalyse the  $H_2$   $WO_3$  reaction. This Pt layer has a high absorption and is preferably far away from where the light mode is located. Figure 3.10 shows that as the Pt layer is close to the Si, the Q factor is low and that when the Pt layer is moved away from the Si (the  $WO_3$  layer becomes thicker), the Q factor increases. In this figure, the Q factor is very low. This is because in the simulation a Pt layer of 20 nm is used which drastically decreases the overall Q factor in the simulation. In practice the Pt layer won't be 20 nm thick but a collection of nanoparticles scattered on the surface as mentioned in the beginning of this section.

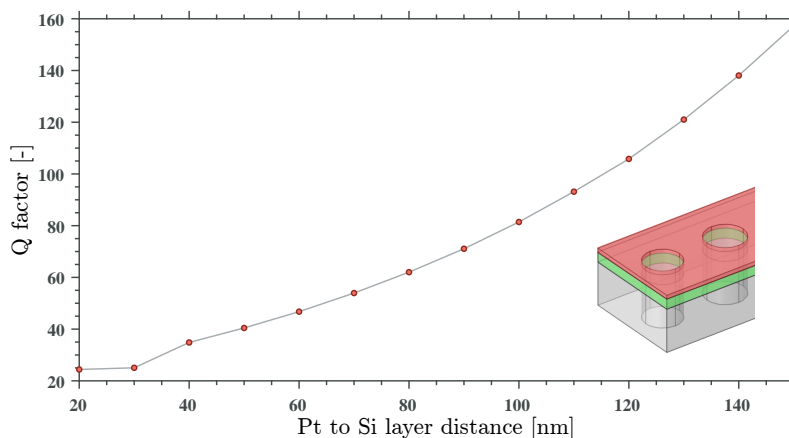


Figure 3.10: The Q factor of a Si (grey) nanobeam with a  $WO_3$  (green) and 20 nm Pt layer (red) on top versus the  $WO_3$  layer thickness showing that the Q factor increases as the high absorption Pt layer is moved away from the light mode.

From this analysis is concluded that for a thicker layer of  $WO_3$  the figure of merit increases. Next to that, the Pt layer is moved further away from the cavity mode which is also favourable for the Q factor. This means that the  $WO_3$  layer needs to be as thick as possible for which the reaction time performance target can still be met.

### 3.3. The Flow of the Results Section

To simulate the performance of the sensor, we would ideally simulate the nanobeam with a  $WO_3$  layer and all Pt nanoparticles, figure 3.11a. However, the feature size of these nanoparticles (< 10nm) is significantly smaller compared to the feature size of the nanobeam making this high aspect ratio simulation extremely

computationally expensive and only possible for a limited number of nanoparticles with the available computational power. To overcome this, we have found a way to incorporate the behaviour of the nanoparticles in the  $\text{WO}_3$  layer to eliminate the need for simulating a lot of nanoparticles. We do this by creating a  $\text{WO}_{3\text{int}}$  layer, where we modify the simulated optical properties to incorporate the effect of the nanoparticles, figure 3.11b. The behaviour of the nanoparticles that is incorporated in the  $\text{WO}_{3\text{int}}$  layer, is obtained by simulating a single nanoparticle. Next to that, the nanobeam with a limited number of nanoparticles is also simulated. Both outcomes are compared and translated to obtain the most accurate  $\text{WO}_{3\text{int}}$  layer so that the nanobeam performance can be simulated without having to simulate with a large number of nanoparticles. In figure 3.12, this structure is given as a flowchart.

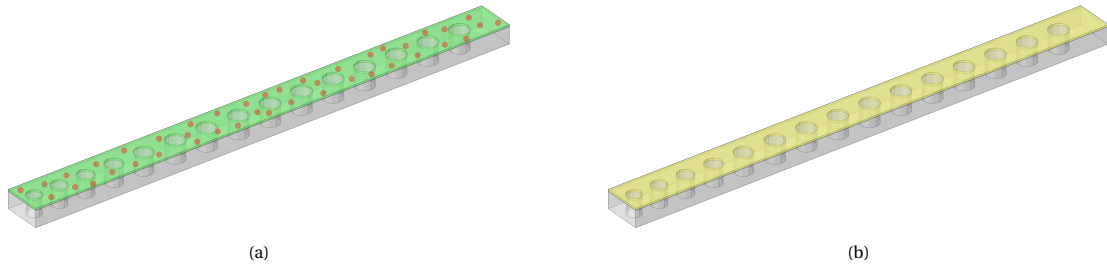


Figure 3.11: The right-half of a Si nanobeam with an (a)  $\text{WO}_3$  (green) and Pt (red) layer and (b)  $\text{WO}_{3\text{int}}$  layer (yellow) where the Pt behaviour is integrated in the  $\text{WO}_3$ .

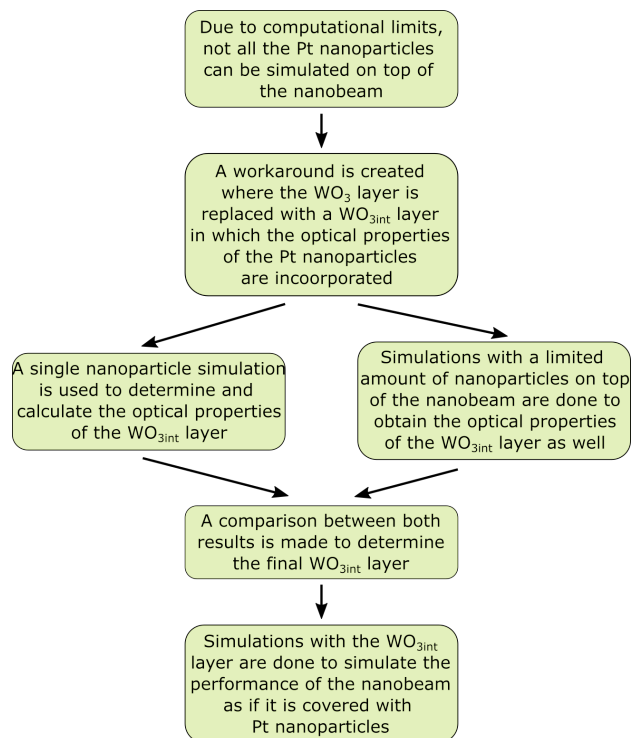


Figure 3.12: A flowchart illustrating how the performance of the sensor is simulated as a result of limited computational power.

# 4

## Results

In this section, all the simulations and the results of those are explained and discussed.

### 4.1. Optimization

Figures 4.1a-c show the geometries of the initial design and both optimized designs for the low and high imaginary refractive indices respectively where each design has a 20 nm  $\text{WO}_3$  layer on top. The optimizer has run for 250 iterations and the resulting Q factors are given in table 4.1. The increase in Q factor for the low imaginary design is significantly higher compared to the high imaginary refractive index design which is likely because of two reasons: By having added the high absorption layer, the initial position of the optimization has changed significantly such that the optimizer does not find the same optimum again which is assumed to be the global optimum. A second reason could be that the objective of the optimization becomes less sensitive for parameter changes when there is much absorption and the Q factor is low. The parameter set obtained with the low imaginary refractive index optimization is used further in this research.

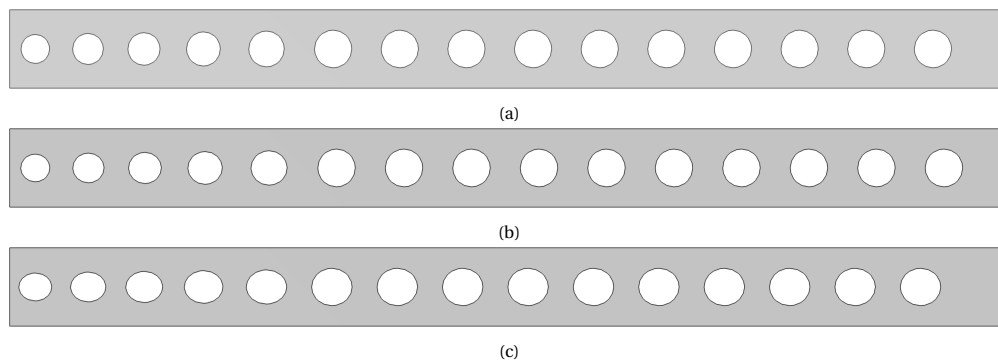


Figure 4.1: Geometries of (a) the initial design, (b) and (c) the low ( $1 \cdot 10^{-6}$ ) and high (0.01) absorption optimized designs respectively.

Table 4.1: The initial and optimized Q factors for a nanobeam with a 20nm  $\text{WO}_3$  layer on top.

Design	Initial Q factor	Optimized Q factor	Relative increase
20 nm low imaginary refractive index $\text{WO}_3$	$9.6 \cdot 10^5$	$1.6 \cdot 10^6$	70%
20 nm high imaginary refractive index $\text{WO}_3$	$7.1 \cdot 10^3$	$7.2 \cdot 10^3$	1.3%

By analysing the parameters as they change through each iteration, more information about the design and the optimization can be found. All of the scaled parameters and the Q factor as a function of the first 120 iterations are plotted in figure 4.2 for the low imaginary refractive index optimization with the final optimal parameters in table 4.2. The percentage in the legend shows how much a variable has changed except for the quadratic parameters as they started from zero. The Q factor plotted in figure 4.2m makes quite a large jump around iteration 20 where it goes from about 1 million to 1.5 million. This large jump is due to small changes in the parameters. Looking at the initial nanobeam design, figure 4.1a and the optimized design, figure 4.1b, the geometries are very similar. Considering the large jump in Q factor for only small deviations in the parameters, shows that when fabricating the sensor, the mechanical tolerance sensitivity is very high. In other words, a small imperfection in the fabrication can lead to a large change in the final performance of the nanobeam which is something to keep in mind when fabricating the sensor.

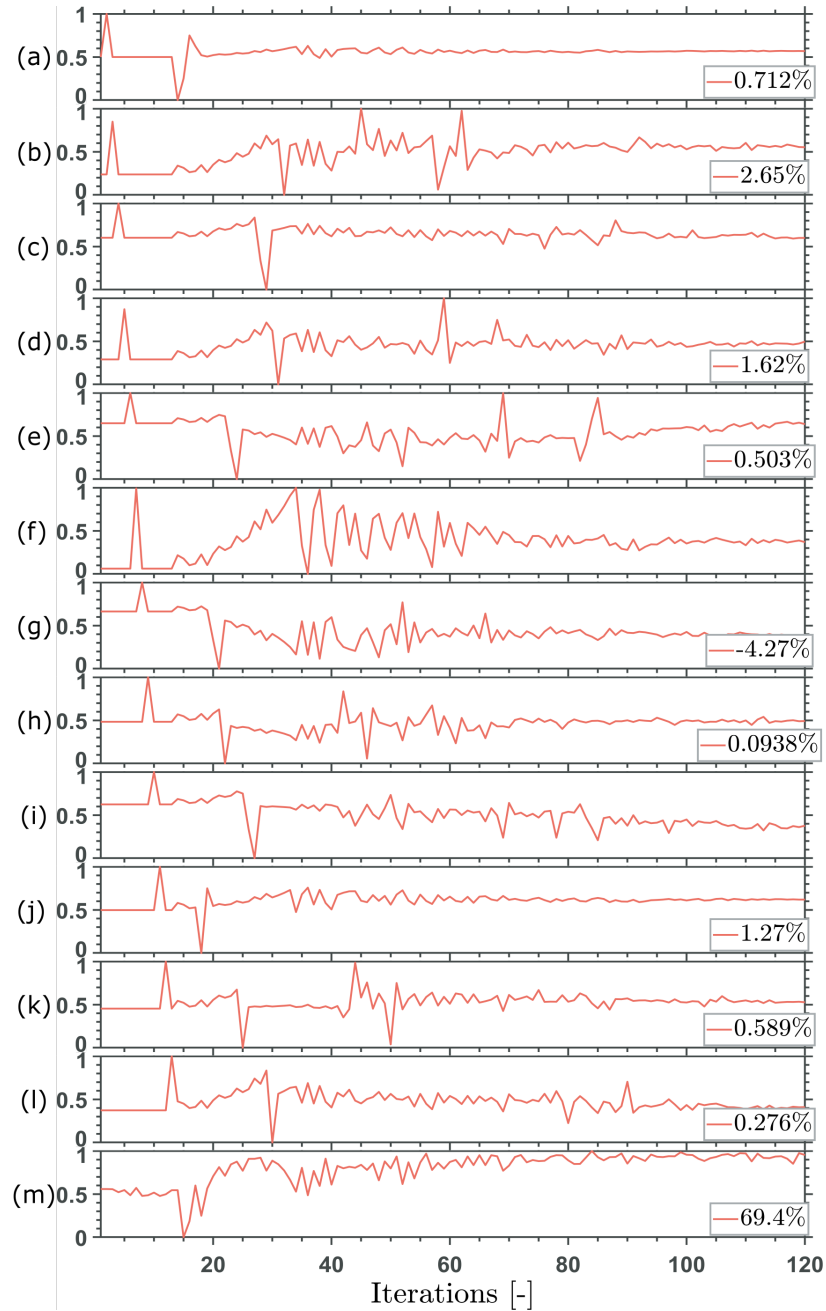


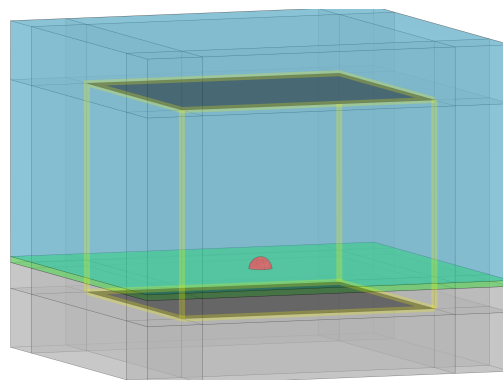
Figure 4.2: All the normalized parameters (a-l) in the order as in table 4.2 and the Q factor (m) plotted versus the iterations of the optimization for a nanobeam with a 20 nm thick  $\text{WO}_3$  layer. The percentage in the legend shows how much percent the parameter has changed.

Table 4.2: The final optimal parameters obtained with the low absorption optimization.

Parameter	Value
$min\_hole\_a$	$0.3324 \cdot 10^{-6} \text{ m}$
$c\_a\_1$	$0.1920 \text{ m}^{-1}$
$c\_a\_2$	$-0.1396 \cdot 10^{-10} \text{ m}^{-2}$
$min\_hole\_x$	$0.9390 \cdot 10^{-7} \text{ m}$
$c\_x\_1$	$0.1457 \text{ m}^{-1}$
$c\_x\_2$	$0.8779 \cdot 10^{-10} \text{ m}^{-2}$
$min\_hole\_y$	$0.8846 \cdot 10^{-7} \text{ m}$
$c\_y\_1$	$0.1451 \text{ m}^{-1}$
$c\_y\_2$	$-0.1788 \cdot 10^{-9} \text{ m}^{-2}$
$mirr\_a$	$0.4355 \cdot 10^{-6} \text{ m}$
$mirr\_x$	$0.1211 \cdot 10^{-6} \text{ m}$
$mirr\_y$	$0.1207 \cdot 10^{-6} \text{ m}$

## 4.2. The Platinum Layer

The Pt layer is a collection of randomly placed nanoparticles on the surface of the nanobeam. The radius is assumed to be 3 nm as derived in section 2.4 resulting in a certain density that describes how many nanoparticles there are per surface varying between  $8.8 \cdot 10^3$  and  $4.4 \cdot 10^4$  particles/ $\mu\text{m}^2$  depending on how much the density scales with the  $\text{WO}_3$  layer thickness. Figure 4.3 shows the single-nanoparticle simulation which is used to analyse the behaviour so that it can be incorporated in the  $\text{WO}_{3\text{int}}$  layer. The simulation consists of a grey Si layer with on top a thin green layer of  $\text{WO}_3$ . The nanoparticle is the red hemisphere on top of the  $\text{WO}_3$ . The simulation is build up such that the domain within the yellow cube is the physical domain and everything around it is a perfectly matched layer. The function of this layer is similar to the scattering boundary condition used for simulating the nanobeam, acting as infinitely far away boundaries. The dark grey surfaces are ports so that the fractional electromagnetic light intensity loss in the particle (red) can be simulated which is the energy absorbed in the particle divided over the energy that is put in the system via the ports. This calculated fractional light intensity loss from the particle simulation can then be translated to extra losses in the  $\text{WO}_3$  layer of the nanobeam simulation by increasing its imaginary refractive index resulting in the  $\text{WO}_{3\text{int}}$  layer.

Figure 4.3: Simulation domain of a Pt particle (red) on top of a  $\text{WO}_3$  (green) and Si (grey) layer in air (blue).

The fractional light intensity loss (an unitless number between 0 and 1) that occurs because of the nanopar-

ticles is due to both scattering and absorption. The absorption losses are very high because Pt has a high imaginary refractive index of 15. The scattering losses are mostly due to Rayleigh scattering which is the scattering that occurs from a collection of nanoparticles where the particle size is much smaller than the wavelength; the dimensionless size of the particle ( $\alpha$ ) is much smaller than 1 [68],

$$\alpha = \frac{2\pi r}{\lambda} = \frac{2\pi \cdot 3 \cdot 10^{-9}}{1550 \cdot 10^{-9}} = 0.012 \ll 1. \quad (4.1)$$

The effect of scattering is assumed to be insignificant compared to the absorption losses which is argued upon in appendix A.1. Therefore the single-nanoparticle simulation is used to obtain the fractional light intensity loss per surface which can be translated to an increased imaginary refractive index for the  $\text{WO}_{3\text{int}}$  layer. Looking at figure 4.4, the varying densities ( $8.8 \cdot 10^3$  to  $4.4 \cdot 10^4$  particles/ $\mu\text{m}^2$ ) as explained in section 2.4 can be visualized as a nanoparticle laying on either a small or large surface of  $\text{WO}_3$  corresponding to a high and low density respectively. If the nanoparticle is taken away from the small piece of  $\text{WO}_3$  it is laying on, that piece of  $\text{WO}_3$  should get a higher imaginary refractive index to account for the absorption losses of the Pt nanoparticle laying on top of it. Comparing the high with the low density, for the high density the surface on which a nanoparticle lays is smaller meaning that the imaginary refractive index should be higher compared to the low density.

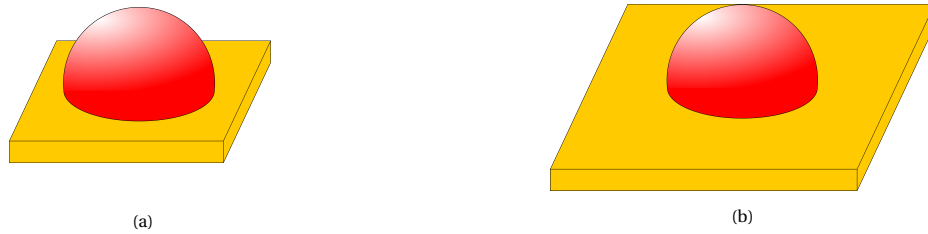


Figure 4.4: A visualization of an (a) high density and (b) low density Pt nanoparticle amount.

To relate the fractional light intensity loss per surface to the imaginary refractive index ( $\kappa$ ) of the  $\text{WO}_{3\text{int}}$  layer, the Beer-Lambert law from section 2.2 is used, (2.3). This equation can be rewritten to  $\kappa$  as a function of the fractional light intensity loss  $F$  and  $x_w$  which is equal to the thickness of the  $\text{WO}_{3\text{int}}$  layer,

$$\kappa = \frac{-\ln\left(\frac{I}{I_0}\right)\lambda}{4\pi x_w} = \frac{-\ln(1-F)\lambda}{4\pi 80 \cdot 10^{-9}}. \quad (4.2)$$

The fractional light intensity loss is a function of the density because a nanoparticle laying on a small piece of  $\text{WO}_3$  (high density) results in more loss than when the particle lays on a larger piece of  $\text{WO}_3$  (low density). Because of this,  $\kappa$  is a function of the density as well, figure 4.5 where equation (4.2) is plotted. With these values for  $\kappa$ , the imaginary refractive index of the  $\text{WO}_{3\text{int}}$  layer is determined. Before doing any Q factor and sensitivity simulations with this layer, in the next section, the nanobeam with a limited number of nanoparticles is simulated as well. Those simulations are used to derive a  $\kappa$  as well and compared to the  $\kappa$  found through the single-nanoparticle simulations to obtain the optimal imaginary refractive index of the  $\text{WO}_{3\text{int}}$  layer.

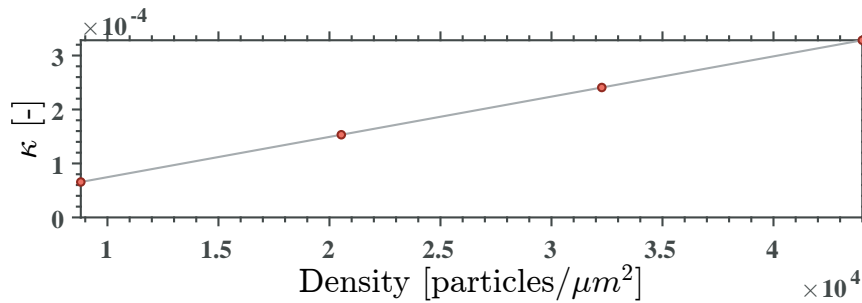


Figure 4.5: The calculated imaginary component of the  $\text{WO}_{3\text{int}}$  layer,  $\kappa$  from equation (4.2), as a function of the density of the nanoparticles on the nanobeam.

### 4.3. Nanobeam with Limited Number of Nanoparticles

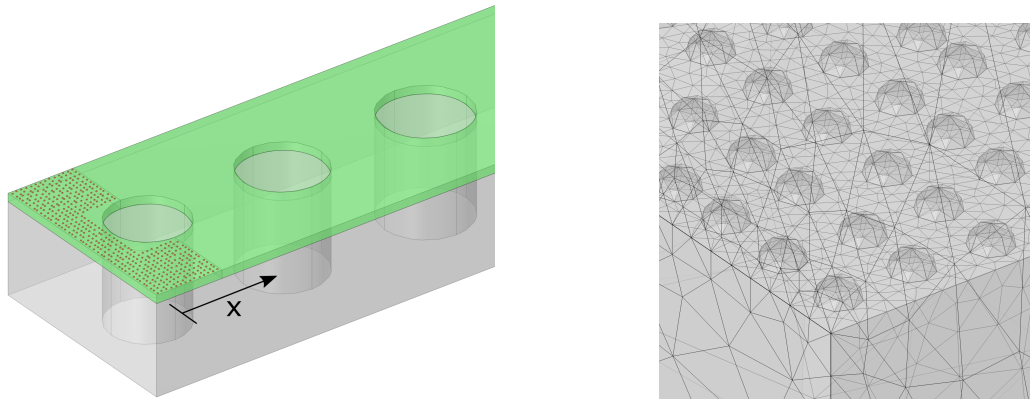
With the right meshing, the nanobeam with a limited number of Pt nanoparticles on top can be simulated, figure 4.6. From the outcome of these simulations, an imaginary refractive index for the  $\text{WO}_{3\text{int}}$  is derived. Together with the single-nanoparticle simulations the right value for the imaginary refractive index is found. Looking at the mesh in figure 4.6b, the radius of the nanoparticles is 3 nm with a minimum element size of 2.5 nm such that the curvature of the particle can still be represented taking any scattering into account showing how fine the mesh becomes. Important to note is that these simulations take hours which makes them unsuitable to do optimizations with. Because only a limited number of nanoparticles can be simulated, the choice is made to place the nanoparticles where the light intensity is the highest, the defect region. This is where the light-matter interaction is the highest. The amount of defect region that is covered is given with  $x$ . The  $\text{WO}_3$  that is not covered with Pt won't change refractive index because without a catalyst, the  $\text{H}_2$   $\text{WO}_3$  reaction is incredibly slow. Next to verifying  $\kappa$ , it is also interesting to see if the sensitivity becomes high enough without compromising the Q factor too much when only the defect region is partly covered with Pt. In the simulation, the nanoparticles are placed on the surface of the nanobeam. At each value of  $x$  there is a row with a fixed number of nanoparticles depending on the density. Per row, the distance between these nanoparticles is not fixed as there is a random offset per nanoparticle. The offset is small enough so that the nanoparticles never touch. The randomness is there to try to approach the randomness at which the nanoparticles are placed on the physical sensor. Due to this randomness, we run the simulation 40 times to determine an average and standard deviation for each performance measure and see how much effect this random scattering of the nanoparticles has on the performance.

In table 4.3, the resulting performances of these simulations are given. For the lowest density ( $8.8 \cdot 10^3$  particles/ $\mu\text{m}^2$ ), the average and standard deviation (in brackets behind the average) is simulated showing that there is some spread because of the random placement of the nanoparticles which is not too large. For higher densities there are more nanoparticles on the nanobeam. Because the computational power is limited, for these higher densities the nanobeam is simulated with slightly larger radius nanoparticles that represent the same amount of Pt volume so that the total amount of nanoparticles didn't become too large.

From analyzing the performance measures in table 4.3, a number of observations are made:

- The Q factor decreases as  $x$  increases because more of the nanobeam is covered with high absorbing Pt. For higher densities the Q factor is lower as well because of the same reason, more Pt on the nanobeam. This makes sense because the Q factor is strongly dependent on the optical losses in the material and because Pt is very absorbing, these losses increase significantly when adding Pt.
- The sensitivity increases for an increasing  $x$  which is also expected because when more of the defect region is covered in Pt, there is more material that changes refractive index when exposed to  $\text{H}_2$ . The found sensitivities for each density are practically the same showing that the sensitivity is not dependent on amount of nanoparticles (absorption) in the nanobeam but solely dependent on the amount of material that changes refractive index,  $x$ .
- The figure of merit increases because the relative decrease in Q factor is less than the relative increase in sensitivity. Interesting to see is if this trend of increasing figure of merit for an increasing  $x$  holds when  $x$  becomes larger than 200 nm. This can be simulated when the  $\text{WO}_{3\text{int}}$  layer is created with the right imaginary refractive index. Important to note is that the figure of merit is calculated with the Q factor for 0%  $\text{H}_2$  which results in a higher figure of merit compared to calculating the figure of merit with the Q factor for 100%  $\text{H}_2$ . The figure of merit is defined with the high Q factor for 0%  $\text{H}_2$  because at these low concentrations it is most interesting to see how well the sensor performs.
- Both the Q factors and sensitivities change a lot for  $x$  going from 50 to 100 nm but less for  $x > 100$  nm which is made more clear by plotting the normalized Q factors and sensitivities in figure 4.7. In the figure, the Q factors for 0%  $\text{H}_2$  and sensitivities for each density are plotted showing that more than 50% of their change in value occurs when  $x$  goes from 50 to 100 nm. The reason for this is that the light intensity is not uniformly distributed on the nanobeam such that the addition of extra nanoparticles (increasing  $x$ ) not always has the same effect. In figure 4.8, the Q factor for a nanobeam is plotted where  $x$  goes from 0 to 1000 nm showing that indeed where the light intensity is high, the Q factor decreases more rapidly. The simulation for this figure is done with a considerably lower nanoparticle density (five

times as small) such that it was computationally possible to simulate for such high values of  $x$ . The absorption of the nanoparticles in this simulation is doubled such that there is significant absorption which is why the Q factors in this plot are not representative. The figure is only there to illustrate the effect of the light intensity distribution on the Q factors and sensitivities.



(a) A  $\text{WO}_3$  layer (green) with Pt nanoparticles (red) on top in the defect region given with  $x$ .

(b) The mesh for the Pt nanoparticles.

Figure 4.6: The nanobeam with an 80 nm thick  $\text{WO}_3$  layer and Pt nanoparticles on top and its mesh.

Table 4.3: The simulated performances of a nanobeam with an 80 nm  $\text{WO}_3$  layer of which only the cavity is covered in Pt nanoparticles given with  $x$  where the mean and the standard deviation (in brackets) are given. The density of the Pt nanoparticles is low,  $8.8 \cdot 10^3$  particles/ $\mu\text{m}^2$ .

density [particles/ $\mu\text{m}^2$ ]	$x$ [nm]	Q factor (0% $\text{H}_2$ ) $10^3$	Q factor (100% $\text{H}_2$ ) $10^3$	Sensitivity [nm/RIU]	Figure of Merit
$8.8 \cdot 10^3$	50	351 ( $\pm 3$ )	13 ( $\pm 1$ )	4.80 ( $\pm 0.02$ )	1088 ( $\pm 10$ )
	100	244 ( $\pm 2$ )	5 ( $\pm 0.7$ )	8.03 ( $\pm 0.04$ )	1262 ( $\pm 12$ )
	150	207 ( $\pm 1.5$ )	5 ( $\pm 0.5$ )	9.52 ( $\pm 0.04$ )	1273 ( $\pm 10$ )
	200	197 ( $\pm 2$ )	4 ( $\pm 0.5$ )	10.9 ( $\pm 0.04$ )	1383 ( $\pm 16$ )
$2.1 \cdot 10^4$	50	112	10	4.86	342
	100	74	5	8.13	351
	150	62	4	9.62	384
	200	48	3	11.0	390
$3.2 \cdot 10^4$	50	53	8	4.90	168
	100	32	3	8.31	173
	150	32	3	9.79	200
	200	28	3	11.1	202
$4.4 \cdot 10^4$	50	31	3	5.10	31
	100	19	3	8.42	124
	150	18	3	9.94	134
	200	9	2	11.4	166

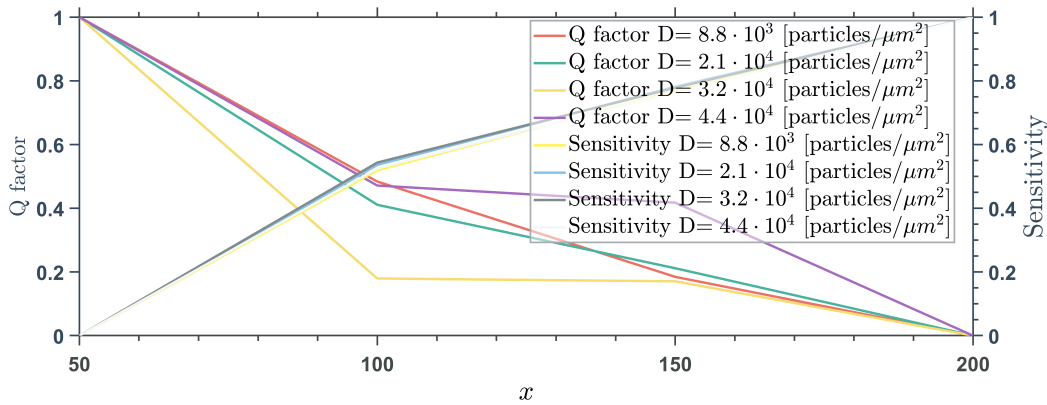


Figure 4.7: The normalized Q factors (going from 1 to 0) and sensitivities (going from 0 to 1) from table 4.3 to illustrate how they change more than half for the first 100 nm because there the light intensity is the highest which results in the most effect went that part is covered in Pt.

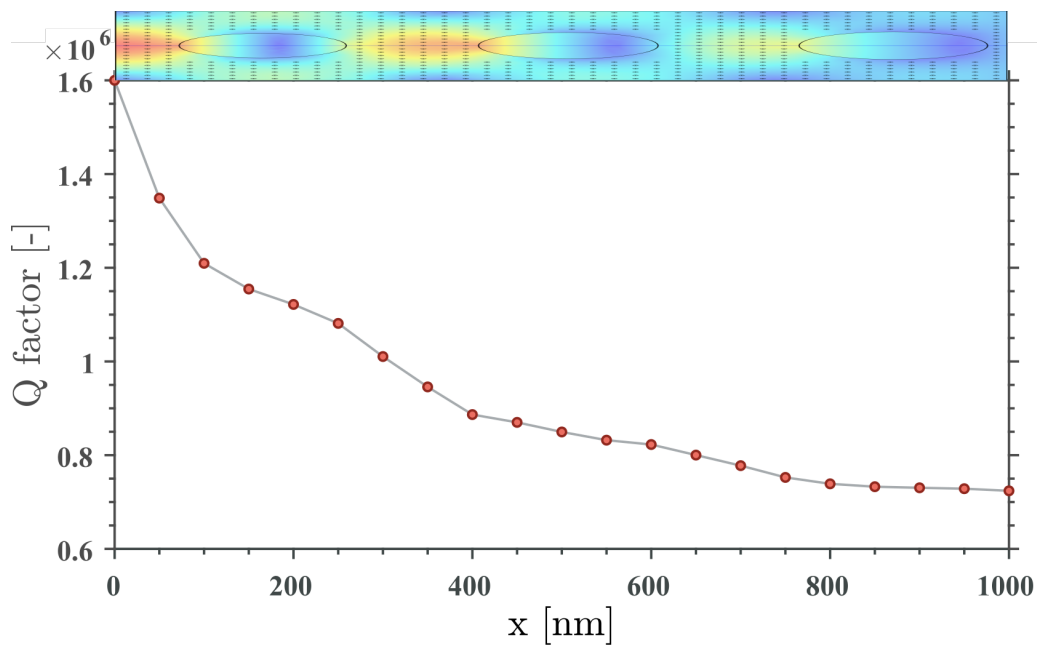


Figure 4.8: The Q factor of a nanobeam showing that it decreases more where the light intensity is high. The nanoparticle density on for this simulation is five times smaller than usual which allows for higher values of  $x$ . Therefore, the resulting Q factors from this plot aren't representative of the actual nanobeam.

## 4.4. Simplified Nanobeam

### 4.4.1. $\kappa$ comparisons

In this section, the right value for  $\kappa$  in the  $WO_{3int}$  layer is decided on based on the single-particle simulations and the simulations with the limited amount of nanoparticles. Figure 4.9 shows the simulation where the  $WO_{3int}$  layer is partially covering the defect region with variable  $x$ . The imaginary refractive index of this layer is obtained by the single-nanoparticle simulations. In figure 4.10, the Q factors as a results of these imaginary refractive indices are plotted together with the Q factors simulated with the limited amount of nanoparticles simulations. The sensitivities are not compared because in section 4.3 was shown that the sensitivity isn't significantly dependent on the absorption.

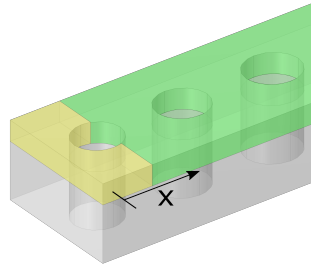


Figure 4.9: Nanobeam with a  $\text{WO}_{3\text{int}}$  layer in the defect region with length  $x$ .

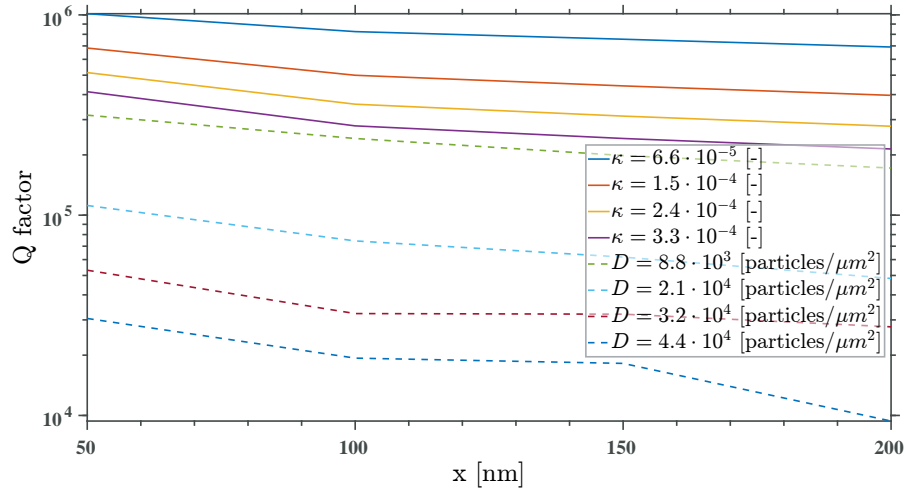


Figure 4.10: The Q factors of different densities as a function of  $x$  for both the simulations with the  $\text{WO}_{3\text{int}}$  layer where  $\kappa$  is obtained through the single-nanoparticle simulations (the first four legend entries) and the Q factors for the total nanobeam simulations where the nanobeam is simulated with a limited number of nanoparticles (the last four legend entries).

Figure 4.10 shows that the Q factors obtained by determining  $\kappa$  through the single-nanoparticle simulations are significantly higher and therefore not an accurate representation of the nanoparticles in the  $\text{WO}_{3\text{int}}$  layer. Therefore, the simulations with the  $\text{WO}_{3\text{int}}$  layer are done again but now with a value for  $\kappa$  such that the Q factors are similar to those found in section 4.3. In figure 4.11 the simulations with the new values for  $\kappa$  are shown with their corresponding values.

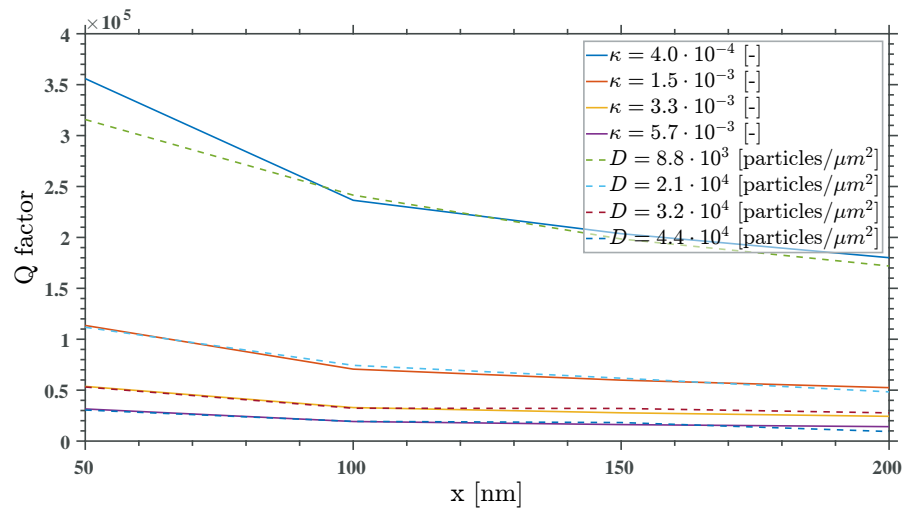


Figure 4.11:  $\kappa$  as originally obtained through the single-nanoparticle simulations is now adjusted so that the resulting Q factors match the Q factors obtained with the limited Pt nanoparticle simulations.

Comparing the new values for  $\kappa$ , figure 4.12, with the old values from section 4.2, figure 4.5, show that  $\kappa$  is significantly higher than previously determined, about an order of magnitude larger. This means that the combination of nanoparticles on the nanobeam have more losses than one nanoparticle multiplied by the total amount. Because Rayleigh scattering was not taken into account for determining  $\kappa$  through the single-nanoparticle simulations, it seems that this simplification has shown to be significant and Rayleigh scattering should have been taken into account as well. Looking at figure 4.12,  $\kappa$  increases more per step in density than  $\kappa$  in figure 4.5, the increase in  $\kappa$  becomes more steep. This makes sense because when looking at  $\kappa$  as a function of the light intensity loss ( $F$ ) from equation (4.2), figure 4.13, the absorption losses in a material increase exponentially meaning that for larger values of  $\kappa$  the curve is more steep.

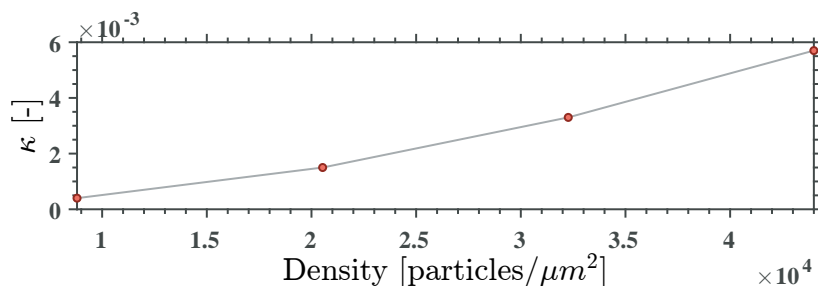


Figure 4.12: The calculated imaginary component of the  $\text{WO}_{3\text{int}}$  layer,  $\kappa$  from equation (4.2), as a function of the density of the nanoparticles on the nanobeam.

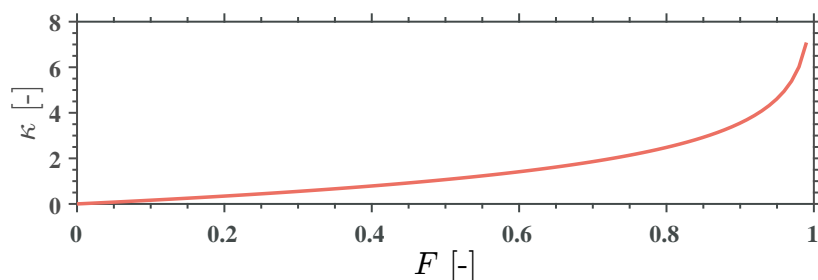


Figure 4.13:  $\kappa$  as a function of the light intensity loss ( $F$ ) according to equation (4.2) illustrating the  $\kappa$  is exponential.

#### 4.4.2. The $\text{WO}_{3\text{int}}$ Layer Simulations

With the new more accurate values for  $\kappa$ , the nanobeam can be simulated for higher values of  $x$  which should, according to the results from section 4.3 result in a higher figure of merit. In figure 4.14, both the Q factor and the sensitivity for each value for  $\kappa$  as a function of  $x$  is shown. The resulting figures of merit increase as expected when  $x$  increases, reaching a maximum at approximately  $x > 2000$  nm.

Because the figure of merit is still just a number, it is also interesting to visualize the wavelength shift that a mode undergoes for 0.1%  $\text{H}_2$ , this is where the refractive index of  $\text{WO}_3$  goes from 2 to 2.0004, figure 4.15. The figures clearly show that for the lowest  $\kappa$ , the modes are quite close to each other and as  $\kappa$  increases, the difference between the modes becomes harder to detect. The result is that measuring 0.1%  $\text{H}_2$  appears to be unrealistic with this specific setup assuming that the Pt density is some value between the minimal and maximum density. Important to remember when reviewing these results is that the  $\text{WO}_3$  layer is 80 nm thick and that the amount of Pt is varied. The values of both parameters are theoretically derived from literature and limited because the reaction time of the sensor needs to be within 1 second. Next to that, the refractive index of  $\text{WO}_3$  is assumed to go linearly from 2.0 to 2.4 when the  $\text{H}_2$  concentration goes from 0 to 100%. However, as shown in section 2.2, the refractive index reaches 2.4 a bit before the  $\text{H}_2$  concentration reaches 100%. Also, the assumption was made that the reaction time decreases linearly with the layer thickness. In practise the decrease in reaction time is probably exponential which could mean that the 80 nm layer thickness could be bigger. In the simulations, the absorption coefficient of the Pt was assumed to be 15 which was also a conservative assumption as some research had estimated the absorption coefficient to be 7. Keeping these assumptions in mind shows that if in practise things like the  $\text{WO}_3$  and Pt layer thicknesses are favourable, the performance of the sensor could meet the 0.1%  $\text{H}_2$  detection target.

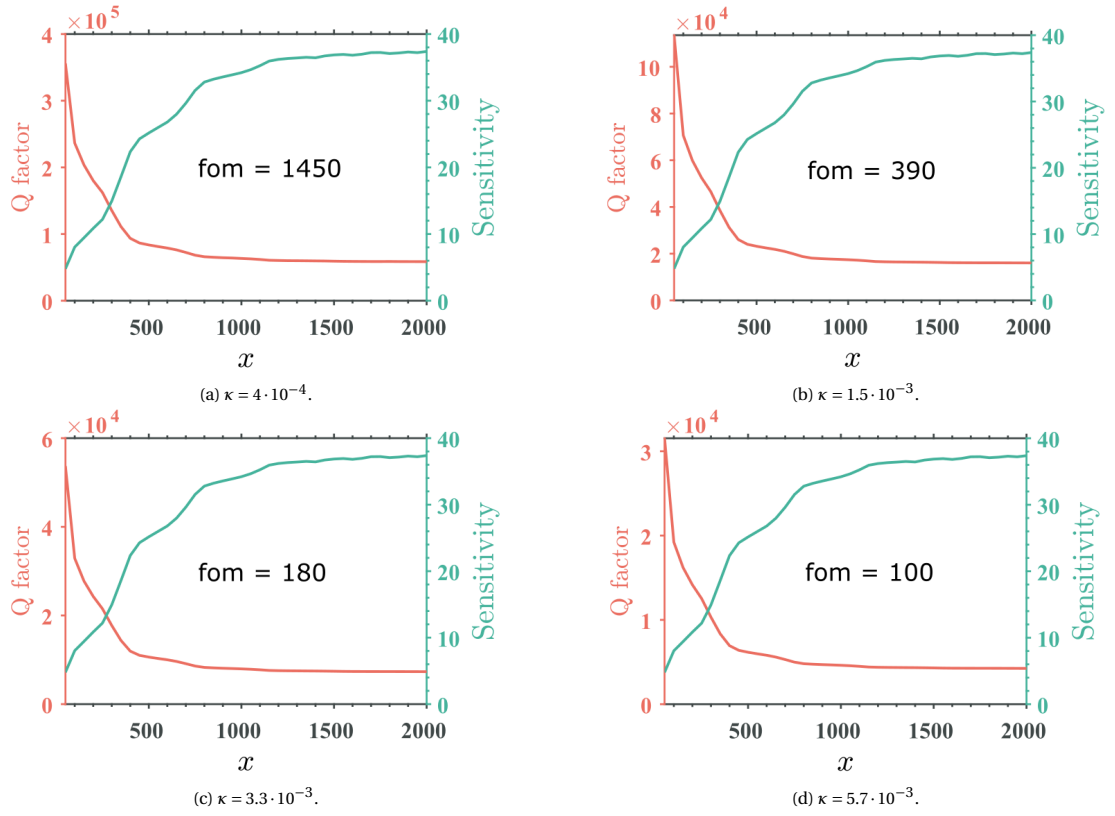


Figure 4.14: The Q factor, sensitivity and maximal figure of merit for the nanobeam with the  $\text{WO}_{3\text{int}}$  layer where the imaginary refractive index ( $\kappa$ ) is varied representing the density. The maximal figure of merit is achieved for  $x > 2000$  nm.

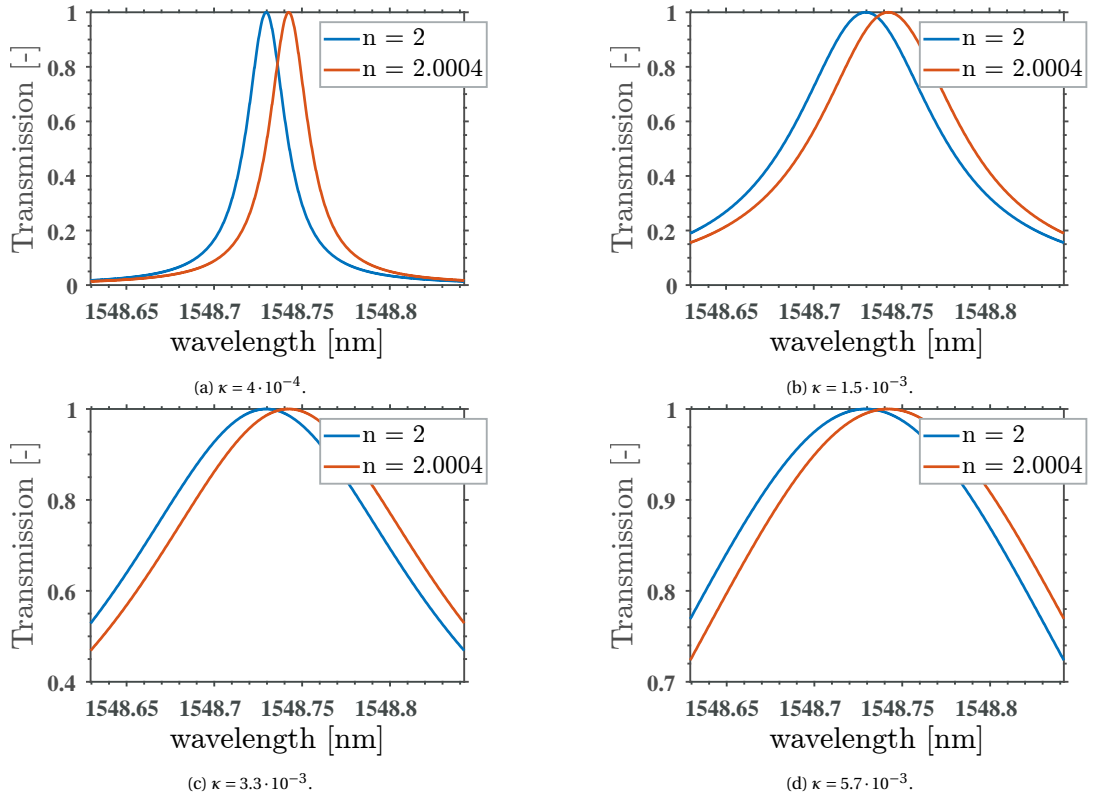


Figure 4.15: The shift in wavelength of the cavity mode after 0.1%  $\text{H}_2$  exposure for the different  $\kappa$  values of  $\kappa$  in the  $\text{WO}_{3\text{int}}$  layer.

## 4.5. Performance Comparison

In order to get an impression of how well the performance of the found design is, it is compared to literature. Because the Q factor, sensitivity and consequently figure of merit are what define the performance of this research, the research to compare with has to be a H<sub>2</sub> resonant refractive index sensor as well so that both the figures of merit can be compared. The best found resonant refractive index sensor found is from Afsari et al. [29] who have simulated a two-dimensional PhC slot-cavity covered with 0.34 nm WO<sub>3</sub> that measures H<sub>2</sub>S instead of H<sub>2</sub>, figure 4.16 which is the same work as mentioned in the introduction of this thesis. Their cavity is a slot-cavity which means that the defect region is a slot-shaped hole (green) where the light intensity is not concentrated in the Si but in the slot. When introducing H<sub>2</sub>S in the defect region, the refractive index of the gas in the slot changes, together with the change of refractive index in the WO<sub>3</sub> is how their sensing mechanism works. They mention that the change of refractive index in the gas due to the H<sub>2</sub>S is very small,  $10^{-4} \frac{nm}{RIU}$ , arguing that it is the change in refractive index of the WO<sub>3</sub> which is responsible for the performance of their sensor. The resulting Q factor is 3000, a change of 0 to 10 ppm H<sub>2</sub>S concentration results in a change of 1 nm in resonance wavelength where 10 ppm is equal to approximately 0.001% H<sub>2</sub>S resulting in a sensitivity of  $2.3 \cdot 10^5 \frac{nm}{RIU}$  and a figure of merit of 2000. Their Q factor is not that high which is reasonable because of the design of their defect region; In a PhC the light energy is concentrated in the high refractive index region, because with their design, they have tried to focus the light intensity to the low refractive index region, it makes sense that it compromises the Q factor. Their sensitivity however, is significantly larger compared to the sensitivity of the nanobeam in this thesis, 40 versus  $2.3 \cdot 10^5 \frac{nm}{RIU}$ . The thickness of their WO<sub>3</sub> is very small (0.34 nm compared to 80 nm) which indicates that they have simulated with different refractive indices as a function of the gas concentration than is done in this thesis. In their paper, they show they have derived their refractive index,

$$2nk = \frac{\sigma}{\omega\epsilon_0} \quad (4.3)$$

where  $n$ ,  $k$ ,  $\sigma$ ,  $\omega$  and  $\epsilon_0$  are the refractive index, extinction coefficient, WO<sub>3</sub> conductance, light source frequency and vacuum dielectric constant respectively. They give  $\omega$  at 0, 5 and 10 ppm of H<sub>2</sub>S resulting in  $2.18 \cdot 10^{-4}$ ,  $1.0 \cdot 10^{-3}$  and  $1.1 \cdot 10^{-3}$  S/cm<sup>2</sup> respectively. Assuming that all the other variables are constant, that shows that  $n$  must increase 5 times for 0 to 5 ppm and stays like that when the concentration goes further from 5 to 10 ppm. This 5 times increase of  $n$  is much larger than  $n$  going from 2.0 to 2.4 for 0 to 100% H<sub>2</sub> as simulated with in this thesis explaining why the sensitivities are so different.

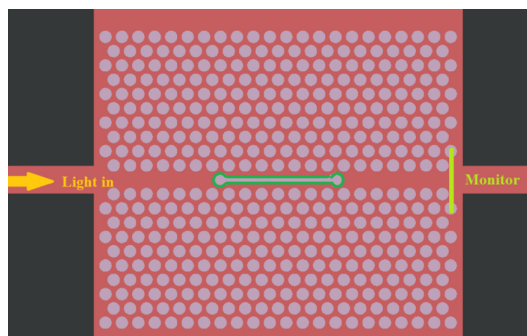


Figure 4.16: The 2D PhC slot-cavity for H<sub>2</sub>S sensing from Afsari et al. [29] made from Si with a 0.34 nm thick WO<sub>3</sub> layer.



# 5

## Conclusion

In this thesis, the performance of a PhC nanobeam cavity as a H<sub>2</sub> sensor is simulated and discussed where the reaction time and figure of merit (a function of the Q factor and sensitivity) are taken into account. The most suitable material for detecting H<sub>2</sub> is WO<sub>3</sub> together with catalyst Pt. The high absorption of the Pt, being a metal, has shown to have a large effect on the Q factor of the cavity mode. Simultaneously, the presence of Pt is necessary for the sensor to meet the 1 second reaction time requirement resulting in a trade-off between the reaction time and the figure of merit and consequently, the minimal H<sub>2</sub> concentration that the sensor can measure.

Not only the amount of Pt, but also the thickness of the WO<sub>3</sub> shows a similar trade-off between the reaction time and figure of merit as for a thicker layer, the sensitivity, thus the figure of merit increases but the reaction time as well. Fortunately, the added WO<sub>3</sub> layer on top of the Si nanobeam only has a small negative effect on the Q factor of the nanobeam meaning that if the reaction time in practise would allow it, the WO<sub>3</sub> layer thickness can become larger, increasing the sensitivity without compromising the Q factor.

The optimizations done with a standard optimization algorithm in Matlab, have shown to increase the Q factor with more than 50%. Analyzing the parameters of this optimization has shown that only small deviations in the parameters can lead to large changes in the Q factor. This shows that when fabricating the sensor, the accuracy at which the holes are etched comes down to nanometers in order to achieve this high Q factor. Because the Q factor plays such a large role in the figure of merit, this is something to be taken into account when fabricating the sensor.

Due to limited computational power, it has not been possible to simulate the nanobeam with all the Pt nanoparticles. Because of this, the optical losses of the Pt are integrated as extra absorption in the WO<sub>3</sub> layer, creating the WO<sub>3int</sub> layer where  $\kappa$  describes the imaginary refractive index of the WO<sub>3int</sub> layer which is responsible for these losses. By simulating a single-nanoparticle, the losses in one particle per surface is obtained. Together with the assumption that the scattering losses are insignificant compared to the absorption losses in the nanoparticle,  $\kappa$  is derived. Simulations with a limited amount of nanoparticles were possible and these results were compared with the values found for  $\kappa$  from the single-nanoparticle simulations. The comparison has showed that the scattering losses from the nanoparticles were actually significant because the values for  $\kappa$  derived in the single-nanoparticle simulations only with the absorption in mind, are one order of magnitude too low.

With the right absorption in the WO<sub>3int</sub> layer representing the losses from the nanoparticles, the performance of the sensor is simulated. Considering that the amount of Pt present needed to achieve the 1 second reaction time is some value between the minimal and maximal density, the minimal detection concentration of 0.1% H<sub>2</sub> is not achieved. However, an optical sensor has no risk of sparks. Its performance is highly dependent on both the WO<sub>3</sub> and Pt layers. If any of these values are more favourable in practise compared to the conservative assumptions made in this thesis; the performance target of a reaction time under one second for H<sub>2</sub> concentrations of 0.1% and higher is feasible.



# A

## Appendix

### A.1. Absorption versus Rayleigh Scattering

Rayleigh scattering, is scattering that occurs from a collection of nanoparticles where the particle size is much smaller than the wavelength; the dimensionless size of the particle ( $\alpha$ ) is much smaller than 1, equation (A.1), also referred to as the Rayleigh regime [68].

$$\alpha = \frac{2\pi r}{\lambda} = \frac{2\pi 3 \cdot 10^{-9}}{1550 \cdot 10^{-9}} = 0.012 \ll 1 \quad (\text{A.1})$$

The optical losses of a particle that lays in the Rayleigh regime, can be described with absorption and scattering losses for  $\alpha \ll 1$ , equation (A.2) [38].  $Q$  is a fraction so it is dimensionless and  $m$  is the complex refractive index of the particle material normalized with the complex refractive index of air, which is practically 1. Filling in the equation gives  $Q_{abs} = 4.1 \cdot 10^{-4}$  and  $Q_{scat} = 5.9 \cdot 10^{-8}$  showing that the scattering losses are significantly smaller than the absorption losses.

$$Q_{ext}(m, \alpha) = Q_{abs} + Q_{scat} = 4\alpha \operatorname{Im} \left\{ \frac{m^2 - 1}{m^2 + 2} \right\} + \frac{8}{3} \alpha^4 \left( \frac{m^2 - 1}{m^2 + 2} \right)^2 \quad (\text{A.2})$$



# Bibliography

- [1] OECD. The Future of Hydrogen: Seizing today's opportunities. Technical report, IEA, Paris, 2019.
- [2] G. Korotcenkov, S. D. Han, and J. R. Stetter. Review of electrochemical hydrogen sensors. *Chemical Reviews*, 109(3):1402–1433, 2009. doi:10.1021/cr800339k.
- [3] I. Darmadi, F. A. A. Nugroho, and C. Langhammer. High-Performance Nanostructured Palladium-Based Hydrogen Sensors - Current Limitations and Strategies for Their Mitigation. *ACS Sensors*, 5(11):3306–3327, 2020. doi:10.1021/acssensors.0c02019.
- [4] U.S. Department of Energy. The Hydrogen and Fuel Cell Technologies Office Multi-Year Research, Development, and Demonstration (MYRD&D) Plan. Section 3.7. *Hydrogen and Fuel Cell Technologies Office*, pages 1–28, 2015.
- [5] Posifa. <https://posifatech.com/>. Accessed: 2022-04-27.
- [6] X. T. Yin, P. Lv, J. Li, A. Jafari, F. Y. Wu, Q. Wang, D. Dastan, Z. Shi, S. Yu, and H. Garmestani. Nanostructured tungsten trioxide prepared at various growth temperatures for sensing applications. *Journal of Alloys and Compounds*, 825(2), 2020. doi:10.1016/j.jallcom.2020.154105.
- [7] G. Mattoni, B. De Jong, N. Manca, M. Tomellini, and A. D. Caviglia. Single-Crystal Pt-Decorated WO<sub>3</sub> Ultrathin Films: A Platform for Sub-ppm Hydrogen Sensing at Room Temperature. *ACS Applied Nano Materials*, 1(7):3446–3452, 2018. doi:10.1021/acsanm.8b00627.
- [8] E. Washizu, A. Yamamoto, Y. Abe, M. Kawamura, and K. Sasaki. Optical and electrochromic properties of RF reactively sputtered WO<sub>3</sub> films. *Solid State Ionics*, 165(1-4):175–180, 2003. doi:10.1016/j.ssi.2003.08.030.
- [9] N. Manca, G. Mattoni, M. Pelassa, W. J. Venstra, H. S. Van Der Zant, and A. D. Caviglia. Large Tunability of Strain in WO<sub>3</sub> Single-Crystal Microresonators Controlled by Exposure to H<sub>2</sub> Gas. *ACS Applied Materials and Interfaces*, 11(47):44438–44443, 2019. doi:10.1021/acsmi.9b14501.
- [10] M. G. Hutchins, O. Abu-Alkhair, M. M. El-Nahass, and K. A. El-Hady. Structural and optical characterisation of thermally evaporated tungsten trioxide (WO<sub>3</sub>) thin films. *Materials Chemistry and Physics*, 98: 401–405, 2006. doi:10.1016/j.matchemphys.2005.09.052.
- [11] M. C. Rao and O. M. Hussain. Optical Properties of Vacuum Evaporated WO<sub>3</sub> Thin Films. *Research Journal of Chemical Sciences*, 1(7):76–80, 2011.
- [12] Z. Chen, K. Hu, P. Yang, X. Fu, Z. Wang, S. Yang, J. Xiong, X. Zhang, Y. Hu, and H. Gu. Hydrogen sensors based on Pt-decorated SnO<sub>2</sub> nanorods with fast and sensitive room-temperature sensing performance. *Journal of Alloys and Compounds*, 811:1–8, 2019. doi:10.1016/j.jallcom.2019.152086.
- [13] M. N. Carcassi and F. Fineschi. Deflagrations of H<sub>2</sub>-air and CH<sub>4</sub>-air lean mixtures in a vented multi-compartment environment. *Energy*, 30:1439–1451, 2005. doi:10.1016/j.energy.2004.02.012.
- [14] S. Matsuura, N. Yamasaku, Y. Nishijima, S. Okazaki, and T. Arakawa. Characteristics of Highly Sensitive Hydrogen Sensor Based on Pt-WO<sub>3</sub>/Si Microring Resonator. *Sensors*, 20(1):96, dec 2019. doi:10.3390/s20010096.
- [15] D. A. Crowl and Y. D. Jo. The hazards and risks of hydrogen. *Journal of Loss Prevention in the Process Industries*, 20(2):158–164, 2007. doi:10.1016/j.jlp.2007.02.002.
- [16] Thorne & Derrick International. Mie minimum ignition energy. <https://www.heatingandprocess.com/product/hazardous-area-zones/mie-minimum-ignition-energy/>. Accessed: 2022-02-03.

- [17] Z. Xie, H. Xu, F. Rong, L. Sun, S. Zhang, and Z. Z. Gu. Hydrogen activity tuning of Pt-doped WO<sub>3</sub> photonic crystal. *Thin Solid Films*, 520(11):4063–4067, 2012. doi:10.1016/j.tsf.2012.01.027.
- [18] D. Nau, R. B. Orzekowsk, A. Seidel, T. P. Meyrath, and H. Giessen. A hydrogen sensor based on metallic photonic crystal slabs. *Optics InfoBase Conference Papers*, 35(18):3150–3152, 2008. doi:10.1364/ol.35.003150.
- [19] Y. Zhao, Q. L. Wu, and Y. N. Zhang. High-Sensitive Hydrogen Sensor Based on Photonic Crystal Fiber Model Interferometer. *IEEE Transactions on Instrumentation and Measurement*, 66(8):2198–2203, 2017. doi:10.1109/TIM.2017.2676141.
- [20] Y. Wang, D. N. Wang, F. Yang, Z. Li, and M. Yang. Sensitive hydrogen sensor based on selectively infiltrated photonic crystal fiber with Pt-loaded WO<sub>3</sub> coating. *Optics Letters*, 39(13):3872–3875, 2014. doi:10.1364/ol.39.003872.
- [21] C. H. Hsu, C. C. Chang, C. M. Tseng, C. C. Chan, W. H. Chao, Y. R. Wu, M. H. Wen, Y. T. Hsieh, Y. C. Wang, C. L. Chen, M. J. Wang, and M. K. Wu. An ultra-fast response gasochromic device for hydrogen gas detection. *Sensors and Actuators, B: Chemical*, 186:193–198, 2013. doi:10.1016/j.snb.2013.06.004.
- [22] D. P. Kulikova, A. A. Dobronosova, V. V. Kornienko, I. A. Nechepurenko, A. S. Baburin, E. V. Sergeev, E. S. Lotkov, I. A. Rodionov, A. V. Baryshev, and A. V. Dorofeenko. Optical properties of tungsten trioxide, palladium and platinum thin films for functional nanostructures engineering. *Optics Express*, 28(21):32049–32060, 2020. doi:10.1364/OE.405403.
- [23] Y. I. Yoon, S. J. Baik, J. P. Mah, and K. B. Hong. Hydrogen sensor based on palladium coated side-polished single-mode fiber. *IEEE Sensors Journal*, 7(12):1767–1771, 2007. doi:10.1109/JSEN.2007.909924.
- [24] T. Hübert, L. Boon-Brett, G. Black, and U. Banach. Hydrogen sensors - A review. *Sensors and Actuators, B: Chemical*, 157(2):329–352, 2011. doi:10.1016/j.snb.2011.04.070.
- [25] M. Green and Z. Hussain. Optical properties of dilute hydrogen tungsten bronze thin films. *Journal of Applied Physics*, 69(11):7788–7796, 1991. doi:10.1063/1.347506.
- [26] Z. Hussain. Dopant-dependent reflectivity and refractive index of microcrystalline molybdenum-bronze thin films. *Applied Optics*, 41(31):6708–6724, 2002. doi:10.1063/1.1461881.
- [27] A. Borgschulte, O. Sambalova, R. Delmelle, S. Jenatsch, R. Hany, and F. Nüesch. Hydrogen reduction of molybdenum oxide at room temperature. *Scientific Reports*, 7(September 2016):1–9, 2017. doi:10.1038/srep40761.
- [28] N. Miyata, T. Suzuki, and R. Ohyama. Physical properties of evaporated molybdenum oxide films. *Thin Solid Films*, 281-282(1-2):218–222, 1996. doi:10.1016/0040-6090(96)08617-8.
- [29] A. Afsari, M. J. Sarraf, and F. Khatib. Application of tungsten oxide thin film in the photonic crystal cavity for hydrogen sulfide gas sensing. *Optik*, 227, 2021. doi:10.1016/j.ijleo.2020.165664.
- [30] J. D. Joannopoulos, S. G. Johnson, J. N. Winn, and R. D. Meade, editors. *Photonic Crystals Molding the Flow of Light*. Princeton University Press, Princeton, 2nd edition, 2007.
- [31] L. Zhuang, X. Xu, and H. Shen. A study on the gasochromic properties of WO<sub>3</sub> thin films. *Surface and Coatings Technology*, 167(2-3):217–220, 2003. doi:10.1016/S0257-8972(02)00904-0.
- [32] M. Penza, C. Martucci, and G. Cassano. NO<sub>x</sub> gas sensing characteristics of WO<sub>3</sub> thin films activated by noble metals (Pd, Pt, Au) layers. *Sensors and Actuators B: Chemical*, 50(1):52–59, 1998. doi:10.1016/S0925-4005(98)00156-7.
- [33] W. C. Hsu, C. C. Chan, C. H. Peng, and C. C. Chang. Hydrogen sensing characteristics of an electrodeposited WO<sub>3</sub> thin film gasochromic sensor activated by Pt catalyst. *Thin Solid Films*, 516(2-4):407–411, 2007. doi:10.1016/j.tsf.2007.07.055.
- [34] F. Cao, P. Zhao, Z. Wang, X. Zhang, H. Zheng, J. Wang, D. Zhou, Y. Hu, and H. Gu. An Ultrasensitive and Ultraspecific Hydrogen Sensor Based on Defect-Dominated Electron Scattering in Pt Nanowire Arrays. *Advanced Materials Interfaces*, 6(1):1–9, 2019. doi:10.1002/admi.201801304.

- [35] N. Tahmasebi Garavand, S. M. Mahdavi, and A. Iraj Zad. Pt and Pd as catalyst deposited by hydrogen reduction of metal salts on WO<sub>3</sub> films for gasochromic application. *Applied Surface Science*, 273:261–267, 2013. doi:10.1016/j.apsusc.2013.02.027.
- [36] S. Kjelstrup, R. Skorpa, S. K. Schnell, and D. Bedeaux. Computing properties of the hydrogen dissociation reaction in and away from equilibrium. *Molecular Simulation*, 42(16):1345–1357, 2016. doi:10.1080/08927022.2015.1117613.
- [37] W. Hoagland, D. K. Benson, and R. D. Smith. Novel Wide-Area Hydrogen Sensing Technology. In *World Hydrogen Energy Conference*, 2007.
- [38] J. H. Seinfeld and S. N. Pandis. *Atmospheric chemistry and physics : from air pollution to climate change*. John Wiley & Sons, Inc., United States of America, third edit edition, 2016.
- [39] S.-M. Jung, S.-W. Yun, J.-H. Kim, S.-H. You, J. Park, S. Lee, S. H. Chang, S. C. Chae, S. H. Joo, Y. Jung, J. Lee, J. Son, J. Snyder, V. Stamenkovic, N. M. Markovic, and Y.-T. Kim. Selective electrocatalysis imparted by metalinsulator transition for durability enhancement of automotive fuel cells. *Nature Catalysis*, 3(August 2020):639–648, 2020. doi:10.1038/s41929-020-0475-4.
- [40] A. D. Rakić, A. B. Djurišić, J. M. Elazar, and M. L. Majewski. Optical properties of metallic films for vertical-cavity optoelectronic devices. *Applied Optics*, 37(22):5271, 1998. doi:10.1364/ao.37.005271.
- [41] W. S. Werner, K. Glantschnig, and C. Ambrosch-Draxl. Optical constants and inelastic electron-scattering data for 17 elemental metals. *Journal of Physical and Chemical Reference Data*, 38(4):1013–1092, 2009. doi:10.1063/1.3243762.
- [42] Q. Qiao, J. Xia, C. Lee, and G. Zhou. Applications of Photonic Crystal Nanobeam Cavities for Sensing. *Micromachines*, 9(11):1–31, 2018. doi:10.3390/mi9110541.
- [43] K. Saurav and N. Le Thomas. Probing the fundamental detection limit of photonic crystal cavities. *Optica*, 4(10):1305, 2017. doi:10.1364/OPTICA.4.000757.
- [44] F. Galeotti, I. Seršić Vollenbroek, M. Petruzzella, F. Pagliano, F. W. Van Otten, Å. Zobenica, A. Moshashami, H. S. Marnani, R. W. Van Der Heijden, and A. Fiore. On-chip waveguide-coupled opto-electro-mechanical system for nanoscale displacement sensing. *APL Photonics*, 5(2), 2020. doi:10.1063/1.5131576.
- [45] D. Yang, H. Tian, and Y. Ji. Microdisplacement sensor based on high-Q nanocavity in slot photonic crystal. *Optical Engineering*, 50(5), 2011. doi:10.1117/1.3574528.
- [46] X. Chew, G. Zhou, H. Yu, F. S. Chau, J. Deng, Y. C. Loke, and X. Tang. An in-plane nano-mechanics approach to achieve reversible resonance control of photonic crystal nanocavities. *Optics Express*, 18(21):22232–22244, 2010. doi:10.1364/oe.18.022232.
- [47] T.-W. Lu and P.-T. Lee. Ultra-high sensitivity optical stress sensor based on double-layered photonic crystal microcavity. *Optics Express*, 17(3):1518–1526, 2009. doi:10.1364/oe.17.001518.
- [48] B. Li and C. Lee. NEMS diaphragm sensors integrated with triple-nano-ring resonator. *Sensors and Actuators, A: Physical*, 172(1):61–68, 2011. doi:10.1016/j.sna.2011.02.028.
- [49] H. Du, G. Zhou, Y. Zhao, G. Chen, and F. S. Chau. Magnetic field sensor based on coupled photonic crystal nanobeam cavities. *Applied Physics Letters*, 110(6), 2017. doi:10.1063/1.4975804.
- [50] S. Sun, H. Kim, G. S. Solomon, and E. Waks. Strain tuning of a quantum dot strongly coupled to a photonic crystal cavity. *Applied Physics Letters*, 103(15), 2013. doi:10.1063/1.4824712.
- [51] I. M. White and X. Fan. On the performance quantification of resonant refractive index sensors. *Optical Express*, 16(2):1020–1028, 2008. doi:10.1364/OE.16.001020.
- [52] A. Di Falco, L. O’Faolain, and T. F. Krauss. Chemical sensing in slotted photonic crystal heterostructure cavities. *Applied Physics Letters*, 94(6):92–95, 2009. doi:10.1063/1.3079671.

- [53] M. W. McCutcheon and M. Loncar. Design of a silicon nitride photonic crystal nanocavity with a Quality factor of one million for coupling to a diamond nanocrystal. *Optics Express*, 16(23):19136–19145, 2008. doi:10.1364/oe.16.019136.
- [54] M. T. Yaseen, Y. C. Yang, M. H. Shih, and Y. C. Chang. Optimization of high-Q coupled nanobeam cavity for label-free sensing. *Sensors*, 15(15):25868–25881, 2015. doi:10.3390/s151025868.
- [55] C. Schinke, P. Christian Peest, J. Schmidt, R. Brendel, K. Bothe, M. R. Vogt, I. Kröger, S. Winter, A. Schirmer, S. Lim, H. T. Nguyen, and D. Macdonald. Uncertainty analysis for the coefficient of band-to-band absorption of crystalline silicon. *AIP Advances*, 5, 2015. doi:10.1063/1.4923379.
- [56] Y. Zhang, M. W. McCutcheon, I. B. Burgess, and M. Loncar. Ultra-high-Q TE/TM dual-polarized photonic crystal nanocavities. *Optics Letters*, 34(17), 2009. doi:10.1364/ol.34.002694.
- [57] Q. Quan, P. B. Deotare, and M. Loncar. Photonic crystal nanobeam cavity strongly coupled to the feeding waveguide. *Applied Physics Letters*, 96(20):17–20, 2010. doi:10.1063/1.3429125.
- [58] Q. Quan and M. Loncar. Deterministic design of wavelength scale, ultra-high Q photonic crystal nanobeam cavities. *Optics Express*, 19(19):18529–18542, 2011. doi:10.1364/oe.19.022191.
- [59] A. Bazin, R. Raj, and F. Raineri. Design of silica encapsulated high-Q photonic crystal nanobeam cavity. *Journal of Lightwave Technology*, 32(5):952–958, 2014. doi:10.1109/JLT.2013.2295267.
- [60] P. B. Deotare, M. W. McCutcheon, I. W. Frank, M. Khan, and M. Lončar. High quality factor photonic crystal nanobeam cavities. *Applied Physics Letters*, 94(12), 2009. doi:10.1063/1.3107263.
- [61] P. Lalanne, S. Mias, and J. P. Hugonin. Two physical mechanisms for boosting the quality factor to cavity volume ratio of photonic crystal microcavities. *Optics Express*, 12(3):458, 2004. doi:10.1364/opex.12.000458.
- [62] Y. N. Zhang, Y. Zhao, and R. Q. Lv. A review for optical sensors based on photonic crystal cavities. *Sensors and Actuators A: Physical*, 233:374–389, 2015. doi:10.1016/j.sna.2015.07.025.
- [63] D. Q. Yang, B. Duan, X. Liu, A. Q. Wang, X. G. Li, and Y. F. Ji. Photonic crystal nanobeam cavities for nanoscale optical sensing: A review. *Micromachines*, 11(1), 2020. doi:10.3390/mi11010072.
- [64] T. Li, D. Gao, D. Zhang, and E. Cassan. High-Q and High-Sensitivity One-Dimensional Photonic Crystal Slot Nanobeam Cavity Sensors. *Photonics Technology Letters*, 28(6):689–692, 2016. doi:10.1109/LPT.2015.2504722.
- [65] M. Chen, L. Zou, Z. Zhang, J. Shen, D. Li, Q. Zong, G. Gao, G. Wu, J. Shen, and Z. Zhang. Tandem gasochromic-Pd-WO<sub>3</sub>/graphene/Si device for room-temperature high-performance optoelectronic hydrogen sensors. *Carbon*, 130:281–287, 2018. doi:10.1016/j.carbon.2018.01.013.
- [66] C. C. Chan, W. C. Hsu, C. C. Chang, and C. S. Hsu. Preparation and characterization of gasochromic Pt/WO<sub>3</sub> hydrogen sensor by using the Taguchi design method. *Sensors and Actuators, B: Chemical*, 145(2):691–697, 2010. doi:10.1016/j.snb.2010.01.021.
- [67] C. Lagarias, Jeffrey, A. Reeds, James, H. Wright, Margaret, and E. Wright, Paul. Convergence Properties of the Nelder-Mead Simplex Method in Low Dimensions. *SIAM Journal on Optimization*, 9(1):112–147, 1998. doi:10.1137/S1052623496303470.
- [68] C. E. Barnett. Some Applications of Wave-Length Turbidimetry In The Infrared. *The Journal of Physical Chemistry*, 46(1):69–75, 1941.